Chapter 4. Antennas and Wireless Power Transfer for Brain-implantable Sensor Devices

Leena Ukkonen, Lauri Sydänheimo, Toni Björninen and Shubin Ma
Faculty of Medicine and Health Technology, Tampere University, Tampere, Finland

4.1 Introduction

4.2 Implantable Antennas for Wireless Biomedical Devices

4.3 Wireless Power Transfer Techniques for Implantable Devices
- **4.3.1** Inductive Power Transfer
- **4.3.2** Ultrasonic Power Transfer
- **4.3.3** Near-field Capacitive Power Transfer
- **4.3.4** Far-Field Power Transfer
- **4.3.5** Computing the Fundamental Performance Indicators of Near-Field WPT Systems using Two-Port Network Approach

4.4 Human Body Models for Implantable Antenna Development
- **4.4.1** Comparison of Human Head Phantoms with Different Complexities for Intracranial Implantable Antenna Development

4.5 Intracranial Pressure Sensing System Integrated with Far-field Transmitter Antenna and Near-field Power Transfer Antenna
- **4.5.1** Far-field Antenna for Data Transmission
- **4.5.2** Antenna for Near-field Wireless Power Transfer

4.6 Far-field RFID Antennas for Intracranial Wireless Communication
- **4.6.1** Split Ring Resonator Based Spatially Distributed Implantable Antenna System
- **4.6.2** LC-tank Based Miniature Implantable Antenna

4.7 Conclusion

4.1 Introduction

The first human brain implant can be traced back as early as 1874 when Roberts Bartholow implanted a pair of electrolytic needles into the meninges of his patient Mary Rafferty [1]. At that time, this experiment aroused a storm of ethical controversy and criticism, even though the experimental results revealed the fact that the sensorimotor function of brain is excitable with electric current. Later in the 20th century, the understanding of the brain and the nervous system became progressively precise and effective treatments for neurophysiological diseases were put forward in succession. For instance, in the year 1924, Hans Berger recorded the first human brain electroencephalogram. His discovery of the brain electrical activity directly leaded to the concept of brain machine interface that helps to establish the bi-directional neural pathway between the brain and the external devices for the paralyzed in late 1970s [2, 3]. Nearly concurrently, a neuroprosthetic device was invented to substitute or augment the damaged sensory with an implant electrode array simulating the neural electrical signals, such as the cochlear implant for the patients with sensorineural hearing loss [4]. Meanwhile, a deep brain implant with neurostimulator for directly alternation of brain activity to manage the movement disorders has been approved for clinical implementation around 2000. These deep brain implants treat essential tremor and have significantly improved the life quality of patients with Parkinson's disease, obsessive–compulsive disorder or epilepsy [5]. Typically, the brain implant in treatments for neurological illnesses needs a chronical implantation under the skull either for high-resolution neural signal recording [6, 7, 8], intracranial physiologically parameters monitoring [9, 10, 11] or deep brain stimulation [12, 13, 14]. Currently, implants are often connected with an off-body signal processor via percutaneous cables through a bone anchored socket. This bulky and fragile structure is unlikely a favorable solution for the sake of patients' mobility and safety in a long-term implementation. For this reason, wireless solutions are presently sought for substituting the cable-based data and power transfer between the implants and the off-body devices for achieving safe and cranially concealed solutions that last for a lifetime.

4.2 Implantable Antennas for Wireless Biomedical Devices

The major challenge in developing a wireless brain implant is to establish a stable and efficient trans-cranial wireless link with an integrated implantable antenna. From the perspective of electromagnetics and wireless communications, a human head is a complex dielectric environment comprising biological materials that are dispersive and characterized with relative permittivity and conductivity tens of times higher than materials present in regular electronics devices and wireless signal ambience. In addition, different tissue types are dissimilar in terms of their dielectric properties. Thus, models comprising multiple tissue types are required in electromagnetic modelling of implanted wireless devices. The brain implant typically needs a deep implant depth under the skull, usually up to 15 mm for neural signal recording and even several centimeters for deep brain stimulation. This deep implant depth with the highly lossy intracranial tissues surrounding the implantable antenna will notably limit the antenna's radiation efficiency and overall worsen the efficiency of the wireless link of the implant. To achieve a long-term implementation of the implant and minimize the biological intrusiveness causing

scar tissue aggregating on the implant that potentially affects the implant performance, the implant should meet extreme structural requirements in terms of device miniaturization, thinness, and flexibility. These physical constraints pose even strict requirements on antenna development in terms of antenna form factors and miniaturization.

Near-field communication with inductive links has been long utilized for wireless implants [15]. These wireless implants utilize the inductive coupled antenna pairs for communication: usually one to be implanted and the other one attached on the skin. These antenna pairs are co-optimized for maximizing the inductive coupling strength between them. Since the magnetic field is more resistive to the deterioration caused by the high lossy tissue materials, the wireless link can be efficient and cause less heating in the surrounding tissues. Due to the high efficiency of the inductive link, a near-field communication system is usually combined with wireless power transfer which will be further discussed in the next section. In near-field communication systems, the amplitude of the magnetic field falls off with the third power of the distance from the antenna. Therefore, the operating distance of a near-field antenna is normally limited to several centimeters. As a rule of thumb, the near-field radius of an electrical small antenna is about one wavelength of its operation frequency, to prolong the operation distance of the antenna, a near-field antenna generally works in the low frequency band, for example 5 – 60 MHz for the commercial cochlear implant systems [16]. Due to the relative long wavelength of the operation frequency, the near-field antennas are generally bulky and coil based. Moreover, since the magnetic field only dominates in proximity to the antenna, the near-field link is also sensitive to the misalignment between the antenna pairs. To alleviate the deterioration by this misalignment, the off-body antenna is usually made with even larger size to expand the effective coverage of the magnetic field. The lower frequency band also restricts the bandwidth of the antenna and limits the attainable data rates to a range of only 106 kbit/s to 424 kbit/s [17].

On the other hand, far-field antennas with potentially higher data rates, smaller antenna dimension and longer operation distance have been increasingly adopted in wireless implant development. Currently, a frequency band from 402 MHz to 405 MHz (U.S. FCC) is specifically allocated for Medical Implant Communications Systems (MICS) and the Industrial, Scientific, and Medical (ISM) bands (e.g. 433.05-434.79 MHz in Region 1, 902-928 MHz in Region 2, and 2400-2500 MHz) are recommended for implantable medical devices. Moreover, the radio-frequency identification (RFID) systems based on backscattering radio communication enables ultra-low-power radios that are also a compelling approach for medical implant communications and the RFID frequency bands centered at 866 MHz and 915 MHz. These frequency bands provide wider bandwidth and more flexibility in implantable antenna development.

In the past decade, various techniques to develop the far-field miniature implantable antennas have been proposed and analyzed. Table 4.1. lists some of the implantable antennas with prior arts. Among them, the multi-layer patch antenna and the planar inverted-F antenna (PIFA) are the most extensively studied antenna types. The main reason for their prevalence is their outstanding flexibility in design and well-understood

miniaturization principles. Generally, the patch antenna consists of two conductor planes (a radiation plane and a ground plane) and high permittivity dielectric superstrate and substrate. The high permittivity of the superstrates and substrate shortens the effective wavelength and helps to decrease the antenna size. The radiation plane, as its name implies, is responsible for EM wave radiation, with careful and ingenious arrangement of the slots and the traces on the radiation plane, a patch antenna can offer advanced electromagnetic features, such as the multiband [23], wideband [19] or circular polarized (CP) [18, 21, 90, 93] operations. The ground plane of the patch antenna ensures a good directivity and detuning resistance in the lossy tissue environment. A short pin between the two conductor planes is also commonly used to further decrease the antenna size. For example, in [18], the size of the proposed antenna is successfully decreased to 3% of the wavelength at the operation frequency. Likewise, the PIFA is composed of a ground plane and a parallel planar radiation element that is shorted to the ground by a pin or plate conductor. The PIFA is widely adopted in implantable devices for its small size and good SAR properties. In [94], the authors elaborately outline the procedure of developing the PIFA for implantable applications. Different miniaturization approaches are compared and evaluated. In [95], the authors report a PIFA based on a spiral radiation element and a folded ground. With such configuration, the antenna with a size less than one centimeter was obtained. Besides the patch antenna and the PIFA, a loop antenna, for its good conformability and small electric field in the vicinity of the surrounding tissues [28, 29], is another good option for wireless implants. In [25, 26], two miniature loop antennas were proposed and evaluated with the implant placed as deep as 11 mm in the brain tissue. In [27], a split ring loaded loop antenna was presented for capsule endoscopy with the implant placed 50 mm deep in the abdominal cavity.

TABLE 4.1 Comparison of different implantable antennas.

Ref.	Year	Type	Frequency (MHz)	Dimension	Implant Depth	Dielectric Material	Gain	Stacking Layer	Short Pin	Features
[93]	2014	Patch	2450	$10 \times 10 \times 1.27$ mm^3	4 mm in skin	Rogers 3010	-19.2 dBi	2	Yes	CP
[20]	2017	Patch	1900	$10.2 \times 4.2 \times 0.4$ mm^3	5 mm in head	Rogers 3010	-14.5 dBi	2	Yes	
[21]	2017	Patch	2450	$8.5 \times 8.5 \times 1.27$ mm^3	2 mm in skin	Rogers 3210	-17 dBi	2	No	CP
[18]	2018	Patch	915	$\pi \times (4.7)^2 \times 1.27$ mm^3	4 mm in skin	Rogers 3010	–32.8 dBi	2	Yes	CP
[19]	2018	Patch	2450	$10 \times 10 \times 0.4$ mm^3	4 mm in skin	Rogers 6010	-9 dBi	2	No	Wideband
[23]	2018	Patch	915, 2450	$8 \times 6 \times 0.5$ mm^3	4 mm in skin	Rogers 6010	-28.5 dBi	2	No	Dual-band
[22]	2019	Patch	2450	$10 \times 10 \times 1$ mm^3	12 mm in CSF	Taconic RF-35	−25 dBi	3	No	Broadside Radiation
[94]	2005	PIFA	403	$24 \times 20 \times 2.4$ mm^3	3.8 mm in skin	Rogers 3010	N/A	2	No	
[96]	2008	PIFA	403, 2450	$22.5 \times 22.5 \times 2.5$ mm^3	3 mm in skin	Rogers 3210	-24 dBi (403 MHz) -7.5 (2480 MHz)	2	Yes	Dual-band
[97]	2014	PIFA	403, 2450	$13.4 \times 16 \times 0.835$ mm^3	3 mm in skin	Rogers 3010	-30.5 dBi (403 MHz) -22.2 dBi (2480 MHz)	1	Yes	Dual-band
[95]	2014	PIFA	2450	$8 \times 4 \times 1.27$ mm^3	4 mm in skin	Rogers 3010	-10.7 dBi	2	Yes	
[91]	2015	PIFA	403	$12.5 \times 12.5 \times 1.27$ mm^3	18 mm in muscle	Rogers 3010	-32.49 dBi	2	Yes	
[24]	2019	PIFA	673	$10 \times 10 \times 3.2$ mm^3	50 mm in muscle	FR 4	-29.4 dBi	2	Yes	
[94]	2014	Dipole	403, 2450	$10 \times 10 \times 0.67$ mm^3	3 mm in skin	Rogers 3010	-30.5 dBi (403 MHz) -19.2 dBi (2480 MHz)	2	Yes	Dual-band
[90]	2015	Loop	915	$13 \times 13 \times 1.27$ mm^3	3 mm in skin	Rogers 3010	-32 dBi	2	Yes	CP
[26]	2017	Loop	915	$\pi \times (12.5)^2 \times 3$ mm^3	11 mm in brain	Rogers 4003	N/A	No	No	
[25]	2019	Loop	403	$16 \times 16 \times 1$ mm^3	14 mm in CSF	FR 4	N/A	No	No	
[27]	2019	Loop	307 - 3500	$18 \times 18 \times 3$ mm^3	50 mm in stomach	Rogers 3010	~ -30 dBi	No	No	Wideband

4.3 Wireless Power Transfer Techniques for Implantable Devices

The supply of stable and continuous power is essential to ensure a proper operation of the implant devices. Conventionally, bio-implantable devices use battery as its power source. Even though the recent advances in battery technology have improved the battery's power density with optimized form factors, the lifetime of the battery is still limited and the periodical surgery to replace the battery will increase the hospitalization time and risk the patients' safety. Therefore, powering the implant wirelessly from the external source outside the human body and meanwhile getting rid of the battery have significance in prolonging the implant's service life, decreasing the implant's overall size and most importantly improving the patient's comfort and safety. To establish the wireless power link between the off-body device and the implant, various approaches have been proposed and evaluated, such as the inductive power transfer, ultrasonic power transfer, near-field capacitive power transfer and far-field electromagnetic (EM) radiation based power transfer.

4.3.1 Inductive Power Transfer

Inductive power transfer is the most extensively studied approach to establish the wireless power link between the off-body devices and the implants. Multiple research involving the inductive power transfer system can be found in the literature, including the analyses of the inductive link over bio tissue [35, 36, 37], power link optimization [38] and coil designs [39, 40, 41, 42]. The block diagram in Fig. 4.1 shows a typical structure of the inductive power transfer system that consists of two coils, namely the TX coil placed externally near the skin and the RX coil to be implanted into the tissue environment. The basic mechanism of inductive power transfer is the electromagnetic induction, which is - an applied alternating current to the TX coil generates a time-varying magnetic field, the alternating magnetic flux passing through the RX coil will induct an electromotive force (EMF) across the RX coil. Then, the inducted current on the RX coil can be rectified to power the implant. Table. 4.2 lists several recent inductive power transfer systems for implantable applications.

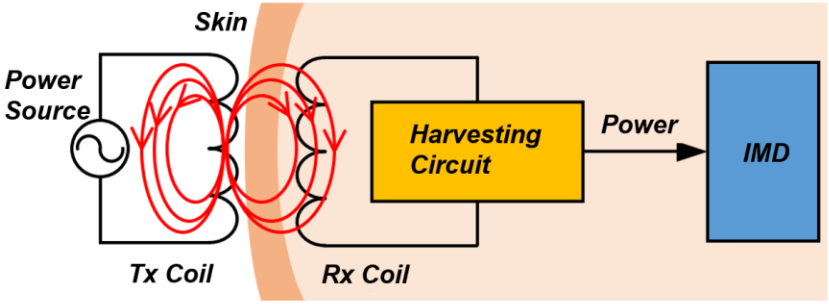

Fig. 4.1 Structure of a inductive power transfer system

As the magnetic field barely interacts with bio tissues, the attainable efficiency of inductive power transfer can be higher than that of the ultrasonic based ones. In [43], the proposed inductive power link reaches an efficiency of 66% with an operation distance of 15 mm in the skin tissue environment. However, since the intensity of the magnetic field decays as $1/d^3$ away from the TX coil, the operation distance is usually limited to 1-

2 centimeter as the RX coil needs to be in the near field of the TX coil for a strong mutual coupling. This implant depth is generally sufficient for subcutaneous implants, however not quite enough for deep implant devices, e.g. the neural implants. To boost the operation range and enables the power transfer to the deep implants, the authors in [44,52,53] developed passive repeaters in between the TX and RX coils to strengthen the mutual coupling between the coils. With such configuration, the attainable operation distance improves to a maximum of 100 mm. Since the tissue loss increases with the frequency, most of the inductive power transfer systems operate in the low frequency band ($\leq$ 20 MHz), the necessary multi-turn coil [54] makes the implant bulky and adds difficulties to implant miniaturization. In [55], the author proved that when the two coils are weakly coupled, for instance, the deep implant with a mm-sized receiving antenna, the power transfer efficiency can be improved by increasing the operation frequency to GHz range when the transmitting antenna is much smaller than the wavelength and sub-GHz when comparable to the wavelength. Based on this finding, several mid-field inductive power transfer systems with a mm-sized receiving antenna were proposed. In [49], a 0.9 mm^3 3D bowtie antenna with a co-designed off-body loop antenna are developed for intracranial power transfer system at 400 MHz. When the bowtie antenna is placed in the CSF layer with an implant depth of 15 mm, a −30.12 dB wireless power link is obtained. In [50], a 2 mm receiving coil with a patterned metal plate antenna is developed for adaptive power transfer to the deep implants at 1.6 GHz. With a 50 mm implant depth in the brain, a -54 dB (0.0006%) power link is established.

TABLE 4.2 Comparison of different inductive power transfer systems.

Ref.	Year	Efficiency (%)	Frequency (MHz)	Received Power	Diameter of Implant Coil	Operation Range	Medium Type
[50]	2014	0.0006	1600	200 μW	2 mm	50 mm	brain
[46]	2015	17	4	20 mW	22 mm	15 mm	rat brain
[45]	2016	13	1.5	15.9 mW	4 mm	110 mm	rat and air
[47]	2016	2.2	20	1.4 mW	1 mm	10 mm	skin
[48]	2016	0.56	200	224 uW	1 mm	12 mm	gray mater
[43]	2017	66	13.56	100 mW	16 mm	15 mm	skin
[44]	2017	2.4	60	N/A	1 mm	16 mm	dura
[52]	2017	0.1	100	N/A	5 mm	50-100 mm	body average
[49]	2018	0.1	400	N/A	1 mm	15 mm	CSF
[51]	2018	1.7	4	N/A	40 mm	30 mm	muscle
[53]	2019	40	5	N/A	35 mm	50 mm	fat
[54]	2019	12.82	100	N/A	2 mm	1.8 mm	skull

4.3.2 Ultrasonic Power Transfer

The ultrasonic power transfer system is generally composed of an off-body transducer, converting the electrical power to the ultrasonic wave, and an implanted receiver, which is usually a microelectromechanical systems (MEMS) based piezoelectric energy harvester. In such a system, the ultrasonic wave transmitted by the off-body transducer (usually an ultrasonic gun) first generates the ultrasonic pressure on the implanted piezoelectric energy harvester. Due to the piezoelectric effect, this mechanical force will

then cause the generation of the internal electric charges and potentials inside the piezoelectric material. The operating frequency of ultrasonic power transfer is usually in a range of 35 kHz to 30 MHz and the attainable maximum operation range can be up to dozens of centimeters with an efficiency up to around 40 % [30]. At the same operation frequency, acoustic wave, due to its low propagation speed, has much shorter wavelength than that of the EM waves. For this reason, ultrasound antennas can be created in a very small dimension to form an antenna array to boost the power transfer efficiency [31]. Moreover, the ultrasonic wave can penetrate conductive materials and has small EM interference to the implanted microsystem. The attenuation of the acoustic wave is proportional to the operation frequency and varies from different tissue types. In most of the human tissues, the attenuation coefficient stays in a range of 1 – 2 dB $cm^{-1}MHz^{-1}$, for example, the attenuation coefficients in muscle and fat are 1.2 and 0.6 dB $cm^{-1}MHz^{-1}$[32], respectively. This low attenuation makes it easy to obtain a deep penetration depth of the ultrasonic wave for subcutaneous implantable applications or even for deep-organ implants, such as the wirelessly powered heart pacemaker and drug pumps [33, 34]. However, due to the large attenuation coefficient in bone (22 dB $cm^{-1}MHz^{-1}$), at a typical operation frequency of 10 MHz, the path loss in skull alone would be more than 100 dB. This considerable attenuation makes the ultrasonic power transfer unlikely an efficient solution for intracranial implantable applications.

4.3.3 Near-field Capacitive Power Transfer

Near-field capacitive power transfer was initially developed as a wireless power transfer scheme for industrial applications. The first exploration of utilizing the capacitive power transfer for implantable applications was reported in [98].

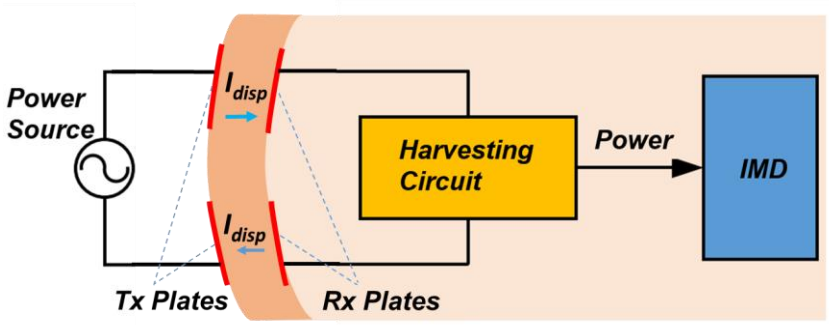

Fig. 4.2 Structure of a capacitive power transfer system

Fig. 4.2 illustrates the basic structure of a capacitive power transfer system, which consists of two pairs of capacitive coupled conductor plates, namely the TX plates placed externally on the skin and the RX plates implanted inside the tissue environment. The TX plates are connected to an AC power source and the power is transferred to the implant through the mutual capacitive coupling between the TX and RX plates in the form of the displacement current across the tissue layer. The operation frequency of the capacitive power transfer system is usually a few MHz to several hundred MHz and the tissue losses (conduction losses and the relaxation losses) are the major factors deteriorating the power transfer efficiency. Since the losses vary with the dielectric properties of the tissue, the operation frequency and the effective area of the plates, the optimization of the capacitive power transfer system requires a comprehensive case-specific considerations. The authors of [99] give a thorough guideline on the optimization of the capacitive power transfer system by modelling the capacitive power link with an equivalent circuit model.

In [99], a flexible subcutaneous capacitive power transfer system is developed. At 98 MHz, with a pair of implanted plates with a size of 20 cm × 20 cm, the power transfer efficiency reaches more than 70 % and the implant depth is 7 mm. Most recently, the authors of [100] developed an intracranial power transfer system based on the resonant capacitive-coupling approach. The developed power transfer system operates at 6.78 MHz. With a pair of 8 mm × 8 mm implantable plates, an implanted intra-cranial pressure sensor was successfully powered. The maximum implant depth reaches 25 mm and the power transfer efficiency is 34%. In comparison with the near-field inductive power transfer, the advantage of the capacitive power transfer is its wide operation bandwidth and smaller detuning affect caused by the flexion of the plates. The limitation of the capacitive power transfer is its relative larger implant size due to the necessity of two implanted plates to form the closed current loop.

4.3.4 Far-Field Power Transfer

The principle of the far-field power transfer is the electromagnetic radiation. In the free space, when the RX antenna is placed in the far-field of the TX antenna, the maximum possible received power by the RX antenna can be calculated with the Friis equation as,

$$P_r = PLF \cdot \frac{P_t G_t G_r \lambda^2}{(4\pi d)^2} \tag{4.1}$$

where P_t is the output power of the TX antenna, G_t is the gain of the TX antenna, G_r is the gain of the RX antenna, d is the distance between TX and RX antennas, and PLF is the polarization loss factor of the wireless link determined by the polarizations of the antennas and their mutual alignment. In implantable application where the RX antenna is implanted inside the lossy tissue environment, the radiation efficiency (and thereby the gain) of the antenna will be significantly reduced as compared to free space environment. The system level of developing the far-field power transfer system for implantable applications and the relevant safety concerns are presented in [95, 101]. In general, the operation frequency of the far-field power transfer system is in the range of a few hundred MHz to several GHz. The operation distance of the far-field power transfer system can be relative longer (a few decimeters) than that of the inductive and capacitive based ones. This longer distance helps communicating with deep implants although the overall link efficiency may not be sufficient for wireless powering of an implant. Moreover, due to the high operation frequency, the RX antenna can be much smaller than that of the near-field based ones. The limitation of the far-field power transfer is its low power transfer efficiency due to the considerable free space power loss, tissue loss and the low radiation efficiency of the electrically small antenna. For example, in [95], the authors evaluated a far-field power transfer system for implantable applications. With an operation distance of 0.3 m and the implant depth of 4 mm in the skin. The power transfer efficiency was only 0.01 % at 2.4 GHz. This makes the far-field power transfer inapplicable for most of the implantable devices. Recently, with the rapid development of the semiconductor industry, RFID based ultra-low power backscattering microsystem are proposed and evaluated for implantable applications. Without of the necessity of the power-consuming active transmitter, the power consumption of the system can be as low as -20 dBm, which opens new possibilities for far-field power transfer in biomedical applications. As a demonstration of this technology, implantable antennas interfaced with a far-field RFID microsystem will be further discussed in section 4.6.

4.3.5 Computing the Fundamental Performance Indicators of Near-Field WPT Systems using Two-Port Network Approach

For a wireless power transfer (WPT) system, maximal power transfer efficiency is normally the most decisive performance indicator that directs the design and optimization of the system. In the near field WPT systems that are the focus of this subsection, the two antennas that establish the wireless link must be co-optimized and cannot be considered as separate entities as in the far field WPT. In the biomedical applications, where the wireless link to a medical implant is through the biological tissue and often complex antenna structures with various material types are involved, closed-form formulas for determining the optimal antenna geometries are not available. Thus, the electromagnetic optimization of these systems is largely based on the full-wave electromagnetic simulations. In this setting, the electromagnetic performance parameters characterizing the system and its power efficiency are most conveniently computed from the linear two-port network parameters that model the general relationship between signals at the input and output of the system.

Below, we summarize the computation of some of the most important performance parameters derived from the two-port impedance parameters (Z-parameters) characterizing the WPT system. The analysis could be based on any other network parameter representation, such as scattering parameters (S-parameters), but as compared with most other network parameters, Z-parameters, which map the port voltages to currents, provide a naturalistic connection to circuit analysis. This is beneficial for analyzing impedances, voltages and currents at nodes of interest within the network.

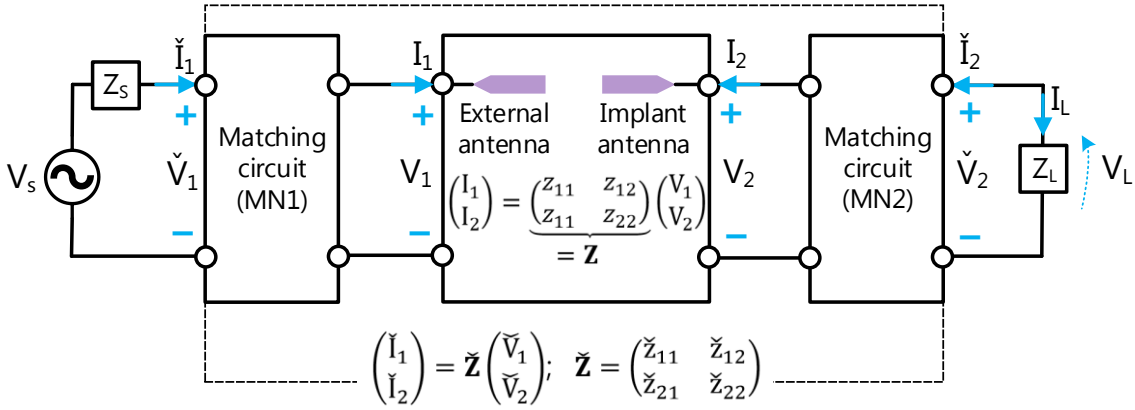

Fig. 4.3 Two-port model of a WPT system.

For further analysis, we consider two sets of Z-parameters as illustrated in Fig. 4.3. The first set of the Z-parameters (Z) models the system comprising the wireless channel and the antennas only, whereas (Z˘) models the complete system including the impedance matching circuits.

In terms of general theory of electronic networks, a WPT system is an unconditionally stable two-port network, because it contains no internal sources of energy. Therefore, it satisfies the following criteria [56, Ch. 2]

$$\begin{cases} 0 < \mathrm{Re}(z_{11}) \text{ and } 0 < \mathrm{Re}(z_{22}) \\ |z_{12}z_{21}| < 2\mathrm{Re}(z_{11})\mathrm{Re}(z_{22}) - \mathrm{Re}(z_{12}z_{21}) \end{cases} \tag{4.2}$$

As we consider only regular non-oscillating and unconditionally stable devices acting as the source and load of the system and passive matching circuits, Eq. (4.2) implies that the input and output impedances that show up at the external and implant antenna terminals are given by [56]

$$Z_{in} = \frac{V_1}{I_1} = z_{11} - \frac{z_{12}z_{21}}{z_{22} + Z_{mn2}} \text{ and } Z_{out} = \frac{V_2}{I_2} = z_{22} - \frac{z_{12}z_{21}}{z_{11} + Z_{mn1}}, \tag{4.3}$$

where Z_{mn2} and Z_{mn1} denote the impedances seen toward the matching networks from the implant and external antennas, respectively.

The upper bound for the total power efficiency of the system is determined by the link power efficiency that depends upon the wireless channel and the antennas only, i.e. the part of the system modelled with **Z** in Fig. 4.3. Thus, it is the ratio of the power delivered to the external antenna to the power available from the implant antenna, which is inclusive of the energy dissipation in the biological tissue, link distance and antenna structures and the related energy dissipation within them and exclusive of the impedance mismatch loss and insertion loss of the matching circuits. The link power efficiency is given by the maximum achievable power gain ($G_{p,max}$) of the two-port network and computed as [56]

$$G_{p,max} = \frac{|z_{21}|^2}{q + \sqrt{q^2 - |z_{12}z_{21}|^2}}, \tag{4.4}$$

where q=2Re(z_{11})Re(z_{22})−Re($z_{21}z_{12}$). We note here that the criterion given in Eq. (4.3) guarantees that the expression inside the square root will be positive. Overall, the link power efficiency computed from Eq. (4.4) is the most crucial performance parameter to be considered in the electromagnetic optimisation of the antenna structures and understand the fundamental limit of the total power efficiency of the system.

The total power efficiency is given by the transducer power gain ($\breve{G}_t$) of the whole system modelled with (**Ž**) in Fig. 4.3. It is the ratio of the power delivered to the load (Z_L=R_L+jX_L) to the power available from the source having the internal impedance of Z_S=R_S+jX_S and computed as [56, Ch. 2]

$$\check{G}_t = \frac{4R_S R_L |\check{z}_{21}|^2}{|(Z_S + \check{z}_{11})(Z_L + \check{z}_{22}) - \check{z}_{12}\check{z}_{21}|^2}. \tag{4.5}$$

This quantity is pertinent for the development of the impedance matching circuits (MN1 and MN2 in Fig. 4.3), following the optimization of the antennas yielding the maximal link power efficiency. The primary target in the circuit development is achieving bi-conjugate impedance matching for maximizing the total power efficiency. This is achieved by first computing the unique pair of impedances Z_{mS} and Z_{mL}, that once connected to the external and implant antenna terminals, respectively, guarantees simultaneously complex conjugate matched interfaces between MN1 and the external antenna as well as the implant antenna and MN2. These optimal antenna terminations are given by [57]

$$Z_{mS/mL} = \frac{\sqrt{q^2 - |z_{12}z_{21}|^2}}{2\mathrm{Re}(z_{22/11})} + j\left(\frac{\mathrm{Im}(z_{12}z_{21})}{2\mathrm{Re}(z_{22/11})} - \mathrm{Im}(z_{11/22})\right), \tag{4.6}$$

where q is as defined in Eq. (4.6). Next, the matching circuits for providing the desired impedance transformation for the given the source and load impedances of the system are designed. In a weakly coupled system where the factor $z_{12}z_{12}$ in Eq. (4.6) approaches zero, the approximations $Z_{mS} \approx z_{11}^*$ and $Z_{out} \approx z_{22}^*$, hold to a good degree of accuracy. In this case, the two matching circuits may be developed independently considering the targets of transforming Z_S to $Z_{mn1} = z_{11}^*$ and Z_L to $Z_{mn2} = z_{22}^*$, which greatly simplifies the circuit development. In both cases, the additional target of the circuit design is using the best practices for component selection and layout design for minimizing the insertion losses of the circuits, so that the total power efficiency ($\check{G}_t$) of the system approaches the link power efficiency ($G_{p,max}$) at the targeted frequency.

In addition to understanding the power efficiency of the WPT system, for the full assessment, we need to know the power delivered to the load as well as the amplitudes of the load voltage and current. Especially the voltage amplitude is an important parameter for voltage activated circuits, such as rectifiers, that are commonly the frontend stage of a remotely powered microsystem being the load (Z_L) of the WTP system. Given the power available from the source ($P_{av.S}$), the power delivered to the load is then obtained as $P_L = G_t P_{avS}$. Finally, Ohm's Law ($Z_L = V_L/I_L$) and the fundamental expression [58]

$$P_L = \frac{1}{2}\mathrm{Re}(V_L I_L^*) \tag{4.7}$$

for computing the time-average load power from the complex load voltage and current phasors, yield the amplitudes of the load voltage and current as follows:

$$|V_L| = \sqrt{\frac{2|Z_L|^2 \widetilde{G}_t P_{avS}}{R_L}} \quad \text{and} \quad |I_L| = \sqrt{\frac{2\widetilde{G}_t P_{avS}}{R_L}}. \tag{4.8}$$

As an example, we consider a wireless link between a miniature loop antenna formed by metallizing four adjacent faces of a 1×1×1 mm^3 sized cube and a planar circular loop with the inner diameter of 12 mm, which has been developed for a wireless brain-machine interface system [59]. In this application, the cubic loop lies on the cortex harvesting energy for a microsystem that records the electrical activity of the brain. The source of energy is a planar loop placed 5 mm above the scalp. As discussed in [59], due to the miniature size of the implanted antenna and the biological environment, the maximum link power efficiency in this system is attained around 300 MHz and thus this frequency was considered for further analysis. This result correlates with other works where it has been established that small implants of the mm-size and below, the optimum frequency lies in the range from 100s of megahertz to low-GHz range [55, 59, 60], whereas in the WPT systems with cm-size and larger implants the operation frequency is typically lower, in the range of 10s of megahertz [61]. The wireless link including the antennas and biological channel was simulated in an anatomical head model of an adult male in ANSYS HFSS for obtaining the impedance parameters **Z** as defined Fig. 4.4. For testing the wireless link, the antennas need to be matched to 50 Ω instruments and thus we set $Z_S = Z_L = 50$ Ω. As expected from the miniature size of the implant, this is a weakly coupled WPT system thus, as can be seen from Fig. 4.5, the approximations $Z_{mS} \approx z_{11}^*$ and $Z_{out} \approx z_{22}^*$ are valid so that the antenna matching networks can be designed independently.

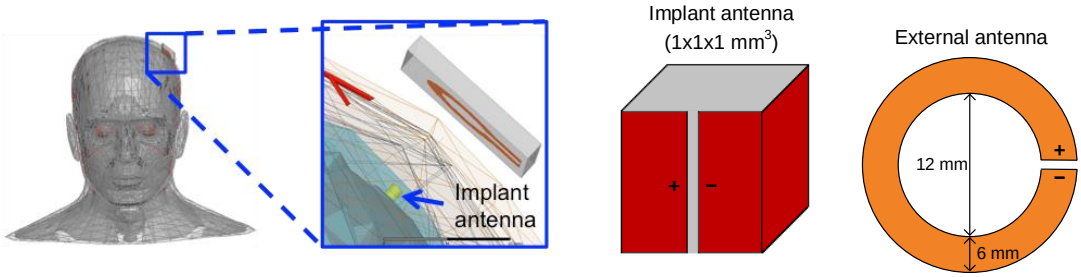

Fig. 4.4. Anatomical model with the implant antenna and the external antenna for WPT

Matching circuits made up of two reactive components, also known as L-networks, can transform any complex impedance to a given resistance [58, Ch. 5.1]. Since our source and load are resistive, we followed this simple approach, where the component values and circuit topologies can be determined from closed-form design formulas presented e.g. [58, Ch. 5.1]. For realizing the matching networks that transform the 50 Ω source and load impedance to $Z_{mn1} = z_{11}^*$ and $Z_{mn2} = z_{22}^*$ at 300 MHz, the following component values were found: C_{mn1} = 13.0 pF, L_{mn1} = 1.80 nH, C_{mn2} = 182 pF, and L_{mn2} = 0.75 nH. Here the capacitors are connected in series with the external and implant antennas and are followed by the inductors in parallel. For practical implementations, it should be noted

that although the component values are feasible for the targeted frequency, the matching circuits that transform the 50 Ω source and load impedances to impedances with notable low resistance are likely very sensitive towards variability due to e.g. component tolerances [62], which is a challenge for building robust systems.

The power transfer characteristics of the studied WPT system are summarized in Fig. 4.6-4.7. The maximum source power for the system is limited the by specific absorption rate (SAR) of the external antenna. In [59], the simulations indicated that under the U.S. FCC safety limit for SAR 1.6 W/kg averaged over one gram of tissue, the maximum P_{avS} for the WPT system is 42 mW at 300 MHz. Considering this limit, the maximum load power is 183 mW with the total power efficiency of −23.5 dB at 300 MHz and the load power remains above 0.1 mW for transmission powers down to 25 mW. Over this range for power transmission, the load voltage and current vary from 100 mV to 135 mV and from 2 mA to 2.7 mA. Overall, the data in Fig. 4.6-4.7, highlights another major challenge for creating biomedical WPT systems with extremely small implants: despite the optimized antennas and operating the system at the frequency of optimal link power efficiency, the power, voltage and current levels available at the implant are pushing the limits of ultra-low-power circuit design required for the implanted microsystems.

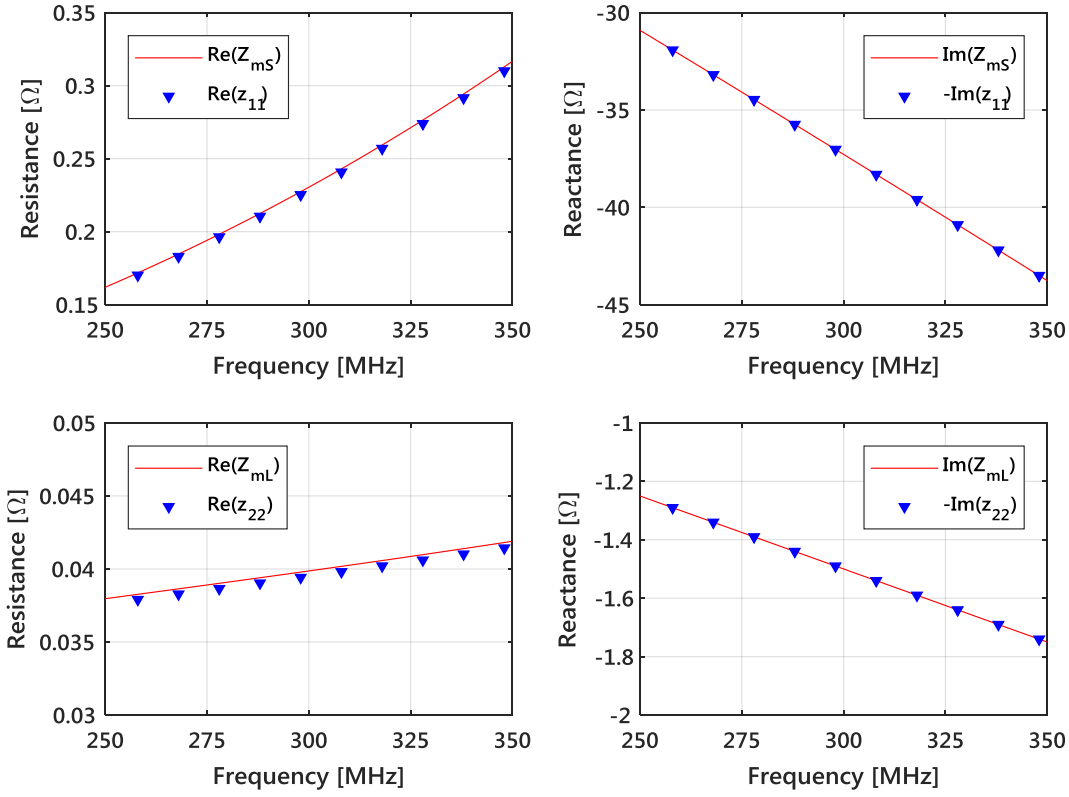

Fig. 4.5. Comparison of the exact and approximated optimum antenna terminations.

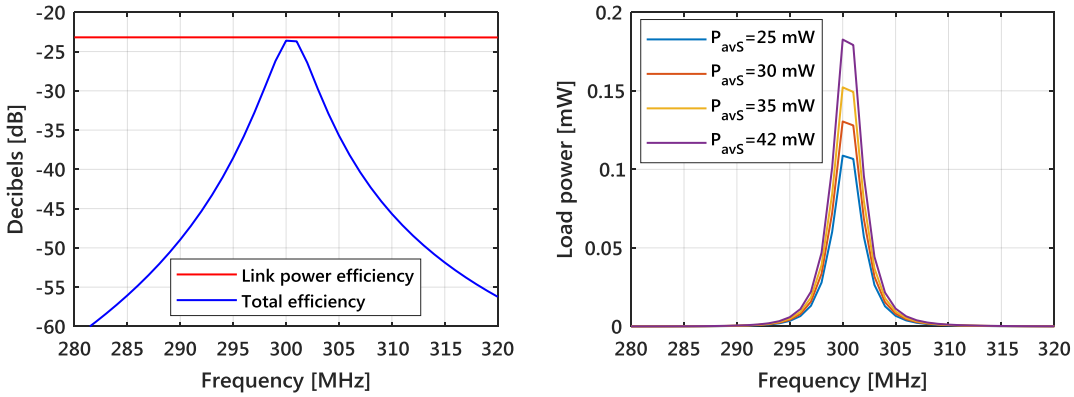

Fig. 4.6. Power transfer efficiency and the time-average load power of the WPT system.

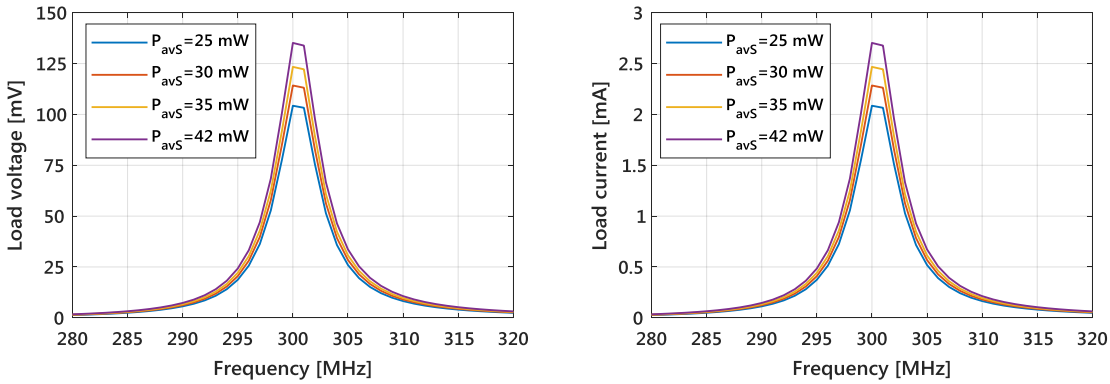

Fig. 4.7. Amplitudes of the load voltage and current.

In summary, the two-port network approach offers a computationally simple framework for characterizing near-field coupled biomedical WPT systems. It is compatible with circuit and field simulation software and experiments with vector network analyser, which both output the two-port network parameters. It can be applied to both weakly and strongly coupled systems and allows holistic computation of the power efficiency parameters as well as estimation for the absolute load power, voltage and current all derived from the network parameters and the given source power.

4.4 Human Body Models for Implantable Antenna Development

In the development of an implantable antenna, computational human body models are indispensable for antenna performance and patient's safety evaluations [63]. On the one hand, the human body models provide the important information on how the surrounding tissue influence the antenna parameters, such as input impedance, radiation efficiency and directivity. On the other hand, the model reflects the tissue reaction to the electromagnetic exposure caused by the antenna radiation. This tissue reaction usually results in the increase of the tissue temperature and may eventually cause tissue damage.

Human body models can be readily made with the CAD tools embedded in the electromagnetic solvers, such as the finite element method (FEM) based ANSYS High Frequency Structure Simulator (HFSS). The canonical models can be made homogeneously with single tissue type or with a layered structure including several different tissue types for a better simulation of a specific implant site of the human body. According to the implant sites, the shape of the models can be cubic, cylindrical or spherical. For example, the seven-layer spherical model with the tissue types of skin, fat, muscle, skull, dura, CSF and brain is commonly used to mimic the layered structure of the intracranial environment. Table. 4.3 lists five layered tissue models for mimicking the intracranial environment. The advantage of these homogeneous and layered models is its low computational complexity. When adopted in the full-wave electromagnetic solver, it saves the computational resource and increase the simulation speed. Moreover, the favourable deformability of the canonical models gives flexibility to investigate the variations of the tissue structures on the antenna performance. The drawback of these models is the limited anatomical adequacy due to their simplified structure. This inadequacy affects the accuracy of the simulation results, especially when evaluating the antenna far field parameters, such as the directivity [64].

TABLE 4.3 Comparison of different human head canonical models.

Ref.	Tissue(s)	Shape (volume)
[66]	skin/tendon/cortical bone	rectangular ($125 \times 87 \times 12.5$ mm^3)
[67]	skin/fat/muscle/skull/dura/CSF/brain	ellipsoid ($10 \times 10 \times 12.5$ mm^3)
[68]	skin/fat/muscle/skull/dura/CSF/gray matter/white matter	rectangular ($75 \times 35 \times 75$ mm^3)
[69]	skin/fat/skull/dura/CSF/brain	spherical ($\pi \times (200)^2$ mm^3)
[70]	skin/fat/skull/brain	rectangular ($100 \times 100 \times 100$ mm^3)

Apart from the canonical models, the anatomical models based on high-resolution medical imaging (e.g. computerized tomography (CT) and digital magnetic resonance images (MRI)) can be adopted to obtain a more accurate estimation of the antenna performance in the tissue environment. Table. 4.4 lists three FEM based anatomical models that can be readily adopted in the HFSS for implantable antenna development.

Meanwhile, a thorough and elaborate survey on the most recent anatomical models can be found in [65]. These anatomical models provide the highly detailed structural information of the human tissue. However, the high complexity also makes them computational heavy and consuming more time in the FEM based electromagnetic solvers. Moreover, since each anatomical model reflects the anatomical details of a certain scanned individual, it is generally impossible to adjust the tissue structure to assess the impact of anatomical variability with the anatomical models.

Before any implementation, the human body model must be augmented with the frequency-dependant tissue dielectric properties (e.g. relative permittivity, conductivity and density). These dispersive dielectric properties can be obtained from the Cole-Cole model or the Debye model. Currently, the IT'IS tissue dielectric database [74], based on the Gabriel's measurements and the four-term Cole-Cole dielectric relaxation model [75, 76], is widely used for the electromagnetic modelling of the human body. This database includes the dielectric properties of 45 human tissues in a frequency range from 10 Hz to 100 GHz. Fig. 4.8 shows the relative permittivity and conductivity of eight major tissue types of the human head from 1 MHz to 10 GHz.

TABLE 4.4 FEM based anatomical human head models.

Ref.	Model Name	Resolution	Region	Entity/Country
[71]	VHP-Female	Variable	Full-body	NEVA EM LLC, WPI, USA
[72]	VHP-Male	Variable	Full-body	NEVA EM LLC, WPI, USA
[73]	BRAIN/SPINAL CORD	1×1×1 mm^3	Head	Universidade de Lisboa, Portugal

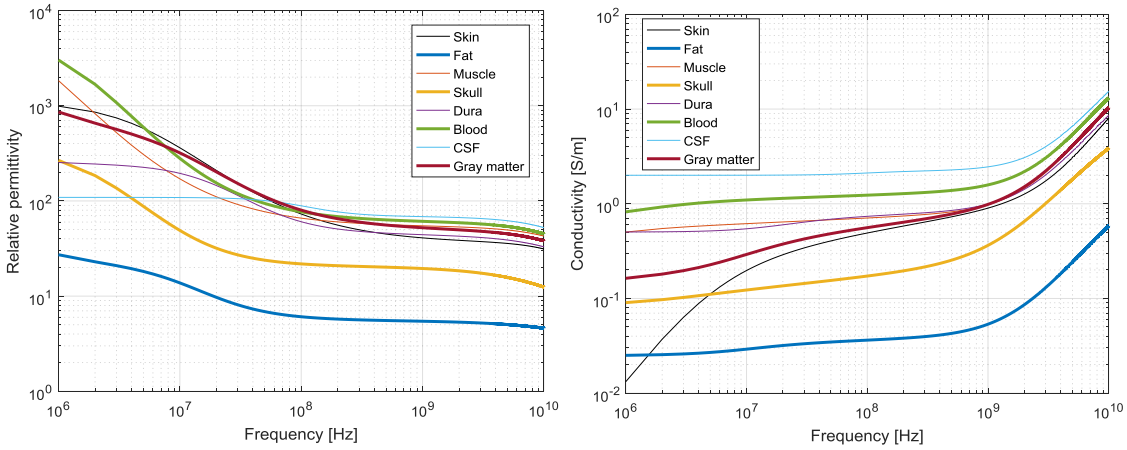

Fig. 4.8 Relative permittivity and conductivity of the major tissue types of human head.

4.4.1 Comparison of Human Head Phantoms with Different Complexities for Intracranial Implantable Antenna Development

The selection of human body model influences not only the computation efficiency but more importantly the accuracy of the simulation results. In this section, we will evaluate different human head models with an identical implantable antenna. The model complexity and the simulated antenna parameters will be evaluated and compared to provide the reader with a reference of the model selection for implantable antenna development.

The antenna [67] selected in this human head model evaluation is developed for the intracranial RFID backscattering system. Fig. 4.9 shows the antenna under test and its dimensions. The antenna consists of wearable and implantable parts. The implant is placed within the CSF (cerebrospinal fluid) and the wearable part is attached on the scalp concentrically. We used the 2 mm thick EPDM (Ethylene-Propylene-Diene-Monomer) (ε_r=1.26, tanδ=0.007 at 915 MHz) as the substrates for the wearable and 50 µm thick flexible polyethylene (ε_r=2.25, tanδ=0.001 at 915 MHz) for the implantable parts. We made the insulation box with silicone (ε_r=2.2, tanδ=0.007 at 915 MHz) with a thickness of 1 mm. In the simulation, we modelled the RFID microchip with a parallel connection of the resistance and capacitance of 2.85 kΩ and 0.91 pF, respectively. We optimized the antenna impedance to achieve a good complex-conjugate matched to the RFID IC in the tissue environment.

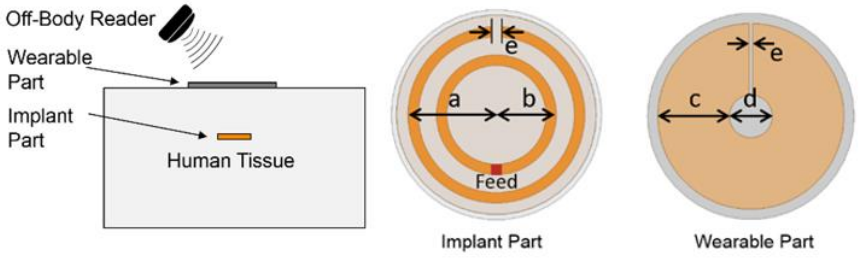

Geometrical parameter (mm)	a	b	c	d	e
	8.6	5.7	20.8	12.6	1.0

Fig. 4.9. Implantable antenna with its geometrical dimensions

The attainable interrogating distance (d_{tag}) given in Eq. (4.9) is the main indicator to evaluate the antenna performance.

$$d_{tag} = \frac{\lambda}{4\pi}\sqrt{\frac{De_r\tau EIRP}{P_{ic0}}}, \quad \text{where} \quad \tau = \frac{4\mathrm{Re}(Z_A)\mathrm{Re}(Z_c)}{|Z_A+Z_C|^2} \tag{4.9}$$

The d_{tag} is inversely proportional to the turn-on power (P_{ic0}) of the IC and proportional to radiation efficiency (e_r), antenna directivity (D), power transfer efficiency (τ) and the equivalent isotropically radiated power limitation ($EIRP$). The power transfer efficiency evaluates the power transfer efficiency from the antenna to the IC, in another words, it quantifies the goodness of the complex conjugate impedance matching between the

antenna and the microchip. Apparently, the d_{tag} is directly influenced by the $e_{r,}$ D, and τ and we will respectively compare these antenna parameters in the four different head models.

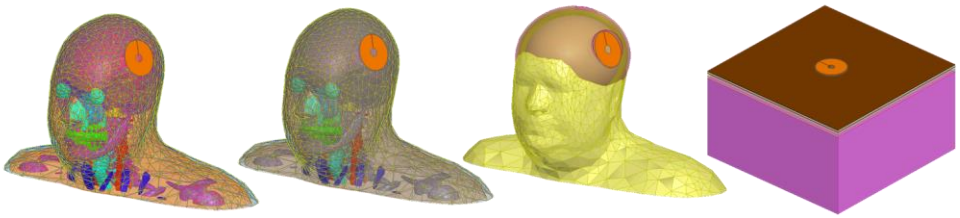

	A	B	C	D
Components	15 individual tissues and 58 separate tissue parts	six major tissue layer - skin, fat, muscle, skull, CSF and brain	six major tissue layer - skin, fat, muscle, skull, CSF and brain	six major tissue layer skin, fat, muscle, skull, CSF and brain
Layer Structure	Original medical image based	Original medical image based	Six-layer ellipsoid replacing the cranial cavity	Six flat block layers 30 mm × 30 mm × 20 mm

Fig. 4.10. Comparison of the evaluated four head models

Fig. 4.10. shows the four human head models in this evaluation. The anatomical head model A is obtained from the open source anatomical VHP-female model [71] which includes 15 individual tissue types and 58 different tissue parts. The model B is a simplified version of the model A. We reduced its complexity by including only six major tissue types: brain, CSF, skull, muscle, fat and skin. We further reduced the model complexity with the semi-anatomical model C, where a six-layer ellipsoid is integrated to substitute the VHP model's cranial cavity. The structure of the six-layer ellipsoid was built as ellipsoid shells with an adjustable thickness representing skin, fat, muscle, skull, CSF and brain. We set the thickness of each layer according to the measurement from the implant location of the VHP model. The model D is a layered box model with a dimension of 30 mm × 30 mm × 20 mm. The box model has the same 6-layer structure as that of the ellipsoid one but all the layers are in a flat form. The dielectric properties of each tissue type is assigned according to the database from IT'IS foundation [74].

The evaluation is conducted with the full wave electromagnetic solver ANSYS HFSS v.17. The computer performed the simulations is equipped with Intel i7 X990 at 3.47 GHz with 24 GB of RAM. In the simulation, the change of the simulated τ, e_r, and D in each iteration is monitored. At six iteration, the solution reached the convergence with the maximum change in τ, e_r, and D are less than 0.01%, 0.14% and 0.13%, respectively, between the subsequent mesh adaptation iterations. Fig. 4.11. compares the number of solved elements and the simulation time (mesh generation and solving 15 frequency points) in the four head models. The simulation speed of the VHP full model is more than six times slower than that of the ellipsoid and block models. The simplified VHP model also has a noticeable reduction of the model complexity and the time consumption.

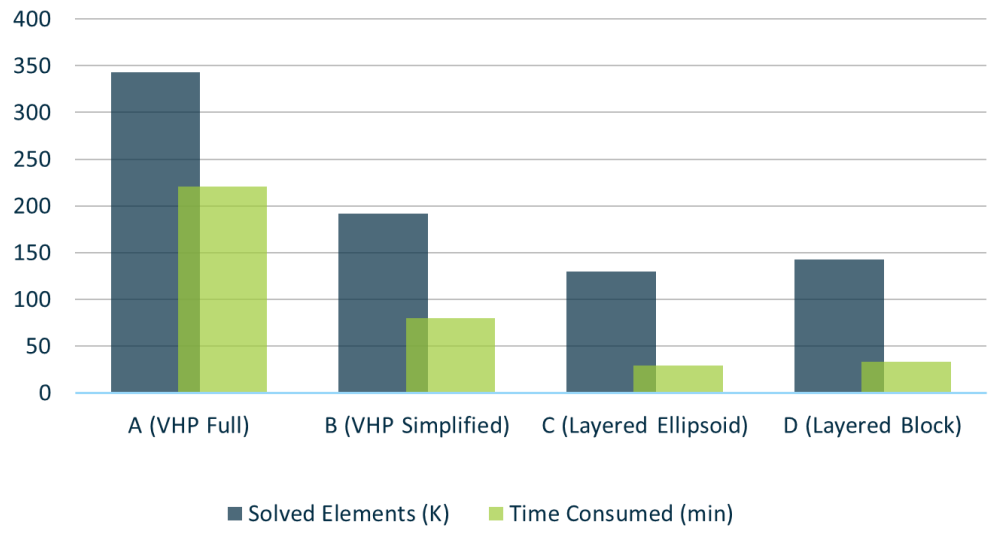

Fig. 4.11. Comparison of the solved elements and time consumption of the four head models.

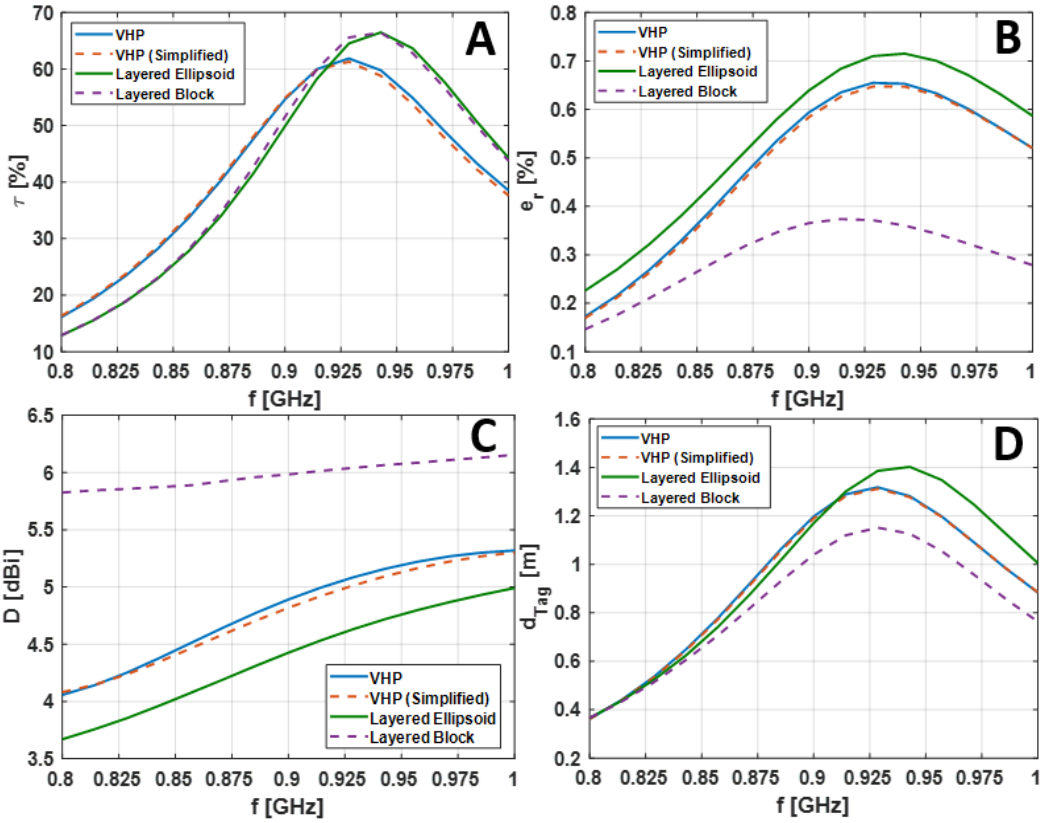

Fig. 4.12. Comparison of the simulated τ, e_r, D and d_{tag} of the four head models.

Fig. 4.12. shows the simulated τ, e_r, D and d_{tag} in the four head models. We considered the results from the VHP full model as the reference model to evaluate the rest models. According to the comparison of the power transfer efficiency τ shown in Fig. 4.12 (A), both the ellipsoid and box models witness a detuning of the peak frequency from 925 MHz to 942MHz. Contrary, the simplified VHP model has an inappreciable influence on

τ. In the comparison of the e_r in Fig. 4.12 (B), the box model has the worst accuracy with detuning of the peak frequency and more than 50% level underestimation, however, the ellipsoid model estimates the peak frequency correctly with less than 10% overestimation of the efficiency level. Fig. 4.12 (C) compares the *D*, the box model is unable to show its variation with the frequency and the level estimation is 1.5 dB less than that from the VHP full model. In contrast, the ellipsoid model, reflects the variation of *D* versus the frequency and level estimation is only 0.5 dB than the VHP full model. Finally, the simulated d_{tag} in the four models is compared in Fig. 4.12 (D). Here, although the box model shows a fine agreement with the VHP full model, it should be mentioned that this agreement is only because of its poor estimation of e_r and *D* compensating each other in the final computation of d_{tag}. Overall, in the estimation of d_{tag}, the simplified VHP model provides nearly the identical results compared with the VHP model and the ellipsoid model has a minor frequency detuning with a small level shift.

According to the simulation results, the layered box model properly estimates the antenna impedance, however fails to provide an accurate estimation of antenna far-field parameters. The layered ellipsoid model not only accurately predicts the antenna impedance but also estimates the far field parameters fair well, moreover the simulation time with the ellipsoid model is less than the box model. For this reason, the box model is not recommended for intracranial antenna development. The anatomical simplified VHP model predicts nearly the same antenna parameters than that of the VHP full model. Therefore, it is not recommended to use the full anatomical model for its redundant anatomical adequacy. The including of dominant layer tissues: skin, fat, muscle, skull, CSF and brain, is enough to obtain accurate results meanwhile to save computational resource. Overall, when developing the intracranial implantable antenna, ellipsoid model is recommended for preliminary antenna optimization and robustness studies where the layer thicknesses are variable and the model complexity is simplified. The anatomical models are more suitable for final verifications of the antenna performance.

4.5 Wirelessly Powered Intracranial Pressure Sensing System Integrating Near- and Far Field Antennas

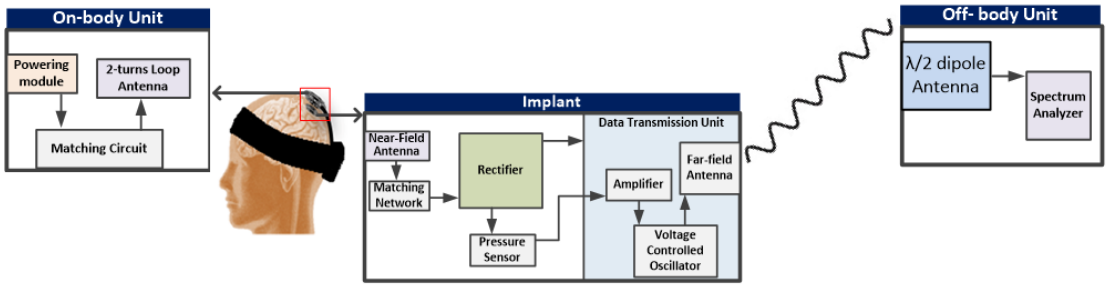

Fig. 4.13. System level description of the pressure sensing system for wireless ICP monitoring

Intracranial pressure (ICP) is defined as the pressure inside the cranial cavity concealing three major volume components; blood, brain tissue and cerebrospinal fluid (CSF). The biological autoregulation of the cerebral blood flow and circulation of CFS maintains the stable ICP below 15 mmHg in adults. The ICP is an important indicator as the dysfunction of autoregulation and/or brain swelling that leads to intracranial hypertension and the increase of the ICP. The excessive ICP impedes the supply of oxygenated blood in the brain and causes brain damage. For this reason, the real time monitoring of intracranial pressure (ICP) plays a crucial role in the management of various brain diseases and injuries [77]. Currently, for the critically ill patients, the ICP is commonly measured from the ventricular system of the brain through a catheter, this method is accurate, allows on-site recalibration as well as drainage of CSF to manage raised ICP, but not fit for long-term monitoring due to its invasiveness with the risk of hemorrhage and infection. Therefore, several studies [78-82] focused on the development of wireless implantable sensors for long-term monitoring of ICP are proposed. Authors of [78] present a battery powered sensor for ICP monitoring at 2.45 GHz. The main limitations of the battery power implantable sensors are the large size and limited life-time due to the battery. To address this limitation, passive ICP sensors are proposed in the literature. In [79], a transcranial implant integrated with the antenna and electronics for wireless monitoring of subdural pressures are proposed and demonstrated. To optimize the footprint of the implant and thus minimize the invasiveness, authors of [80, 81] developed capacitive MEMS based battery-free ICP sensors. These passive devices are small and flexible, however have limited functionality and short operation distance compared with the battery powered sensors. Alternatively, the battery-less ICP sensors equipped with the wireless power harvester is a potential minimally invasive solution to overcome the life-time and size limitation of the battery assisted method and the limited operation distance of the fully passive method. The work in [82] proposes the development of a batteryless wirelessly powered ICP sensor. Fig. 4.13 shows the system architecture of the proposed sensor that consists of in-, on, and off-body units. The in-body unit has four parts including a 2-turns coil antenna for wireless powering, a rectifier for RF-to-DC conversion, a piezoresistive pressure sensor and a data transmission unit. The in-body unit is placed under the skull and powered by the on-body unit through inductive coupling. The piezoresistive pressure sensor has a differential output voltage which is

proportional to the change in the pressure. When activated, this output voltage of the pressure sensor is amplified through an amplifier and drives the voltage control oscillator (VCO). Finally, the far-field antenna connected to the VCO output transmits the pressure readout to the off-body unit.

4.5.1 Far-field Antenna for Data Transmission

As outlined above, our wirelessly powered intracranial pressure sensing system integrates near- and far-field links for the wireless powering and data communication, respectively. Given the application, the development of the whole system is driven by achieving thin and flexible platform with as small as possible overall size. In our case, the size is limited by the size of the inductive loop (discussed in detail in the next subsection) required for achieving adequate power transfer efficiency. With the aim of not increasing the platform size, the far-field antenna and other electronics must fit within the area of the loop. Stemming from these considerations, the required footprint size of the far-field antenna was limited to 6 mm × 5 mm. Due to the thinness of the substrate, we considered only planar antennas and due to the compactness of planar inverted-F antennas among them, we selected this antenna type for further considerations. As shown in Fig. 4.14, we have applied spiral folding on the radiating arm for lowering the resonance frequency to 2.45 GHz. The antenna was simulated and optimized in the ANSYS HFSS v15 with the target of maximizing the realized gain pointing outwards the brain within the constrained area of 6 mm × 5 mm. In the simulation, a tissue model with 4 tissue layers: skin, fat, bone and brain was built to represent the intracranial tissue environment.

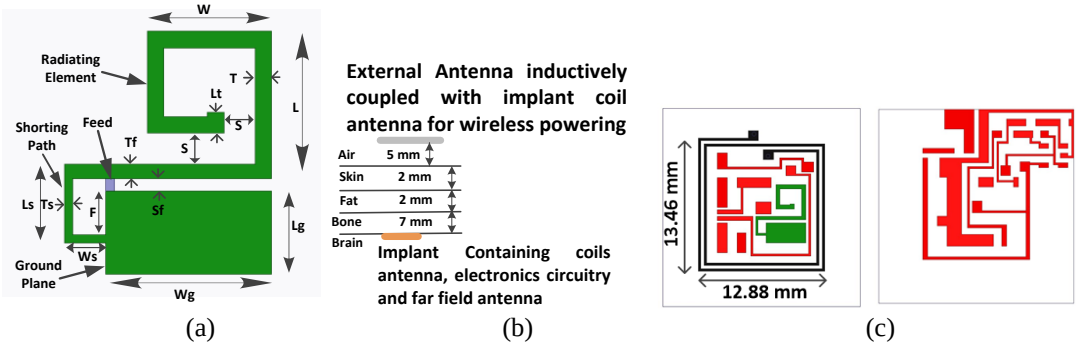

Symbol	L	W	Lg	Wg	Ls	Ws	T	S	Lt	Sf	Tf	F	Ts
Value [mm]	3.55	3	2	4	1.9	1	0.4	0.75	0.5	0.3	0.35	1.05	0.2

Fig. 4.14. (a) Top view of design antenna (b) Cross-sectional view of the tissue model (c) Implant front and back side view (red traces represent electronic circuitry, black represents 2-turns coil antenna and green represents far-field antenna)

Fig. 4.14.(b) shows the structure of the tissue model. The proposed antenna was placed on the sensor platform together with electronics circuit traces as shown in Fig. 4.14. (c). To isolate the antenna from the tissue environment, a silicone coating was made to cover both sides of the antenna. Fig. 4.15. (a) shows the simulated reflection coefficient of the antenna. The -10 dB bandwidth of the proposed antenna in the simulation is 280 MHz

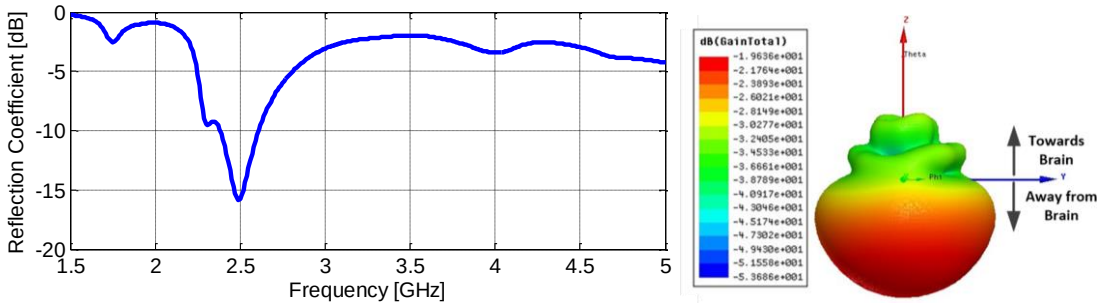

(a) (b)

Fig. 4.15. (a) Simulated reflection coefficient (dB). (b) Antenna 3D gain pattern at 2.45 GHz.

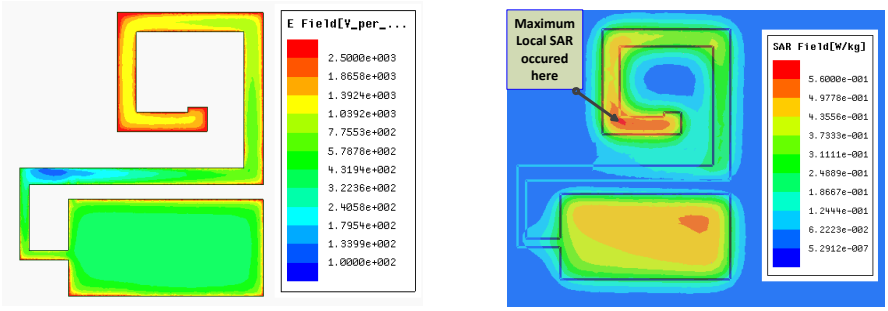

(a) **(b)**

Fig. 4.16. (a) E-field (V/m) distribution at antenna surface (b) Local SAR (W/kg) distribution at bone interface when input power to antenna is 0.5 mW at 2.45 GHz.

(2.21 GHz to 2.49 GHz) and the antenna reflection ecoefficiency at 2.45 GHz is -14 dB. The simulated 3D antenna gain is demonstrated in Fig. 4.15. (b) with peak gain of -19.6 dBi toward the direction away from the brain. The antenna radiation efficiency and directivity at 2.45 GHz are 0.5% and 4.33 dBi, respectively. The SAR estimation of the antenna was conducted using a block phantom ($18.75\times18.75\times30$ cm^3) with only brain and bone tissue. The height of the block was set to 30 cm to accommodate two averaging cubes congaing approximate 1 gram of the brain and bone. Fig. 4.16. (a) shows the E-field distribution at 2.45 GHz. The radiating element of the antenna is acting as a $\lambda/2$ resonator at 2.45 GHz. Fig. 4.16. (b) presents the local SAR distribution at the bone

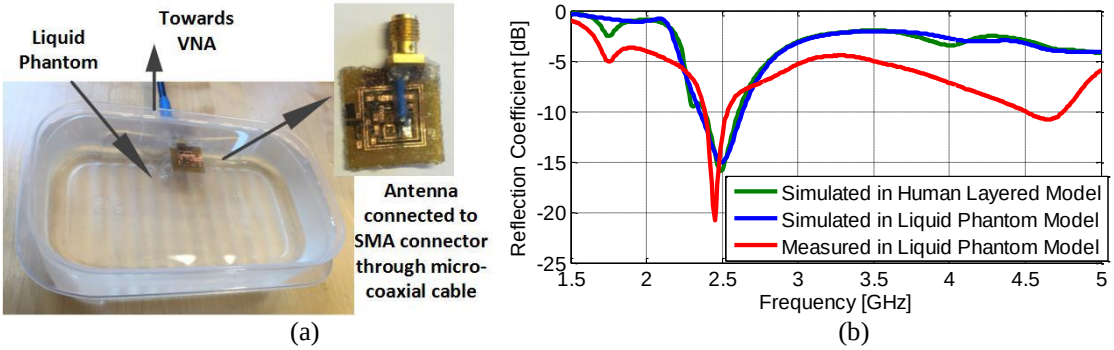

(a) (b)

Fig. 4.17. (a) Reflection coefficient measurement setup and fabricated antenna. (b) Simulated (both human head and liquid phantom) and measured reflection coefficient (dB).

interface. The maximum local SAR value is 0.58 W/kg and the maximum SAR-compliant transmission power is 5.53 mW.

The antenna was manufactured on the flexible polyimide substate for the experimental verifications. Fig. 4.17. (a) shows the prototype and the measurement setup. The liquid phantom (ε_r = 39.2 and σ = 1.8 S/m at 2.45 GHz) made of water, sugar and salt was used to mimic the human head environment [83]. Fig. 4.17. (b) presents the simulated (both human layered and liquid phantom models) and measured reflection coefficients. A good agreement can be found between the simulation and measurement results. The measured -10 dB bandwidth is 160 MHz (from 2.38 GHz to 2.54 GHz) with 20.8 dB return loss at 2.45 GHz. The bandwidth is verified to cover the whole range of the ISM band.

4.5.2 Antenna for Near-field Wireless Power Transfer

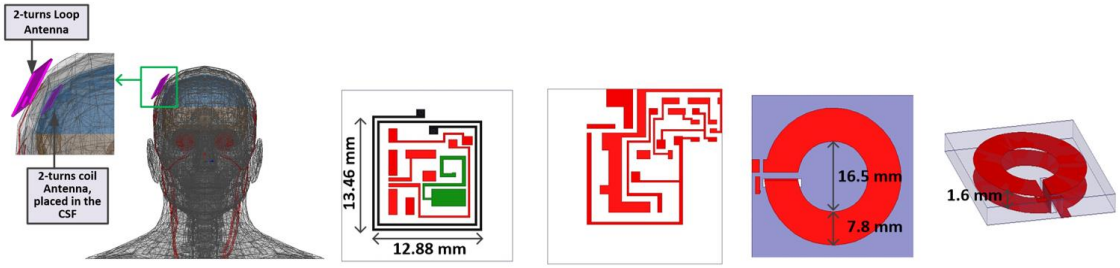

(a) (b) (c) (d) (e)

Fig. 4.18. (a) Anatomical head model in the simulation for wireless link and antenna modeling (b) front side of implant consists of 2-turns coil antenna (black), far-field antenna (green) and traces for other components (red) (c) backside of implant consists of traces for electronic components (d) top view of external antenna (e) side view of external antenna

The wireless power transfer link of the proposed ICP sensor is established by two inductively coupled loop antennas. Fig. 4.18. (b) shows the top side view of the 2-turn RX loop antenna in the in-body unit. This antenna is designed on a 50 μm thick flexible polyimide substrate (ε_r = 3.3 and tanδ = 0.002 at 15 MHz). For biocompatibility, the implant is encapsulated with silicone and Parylene C coating. Fig. 4.18 (d) and (e) shows the 2-turn TX loop antenna in the on-body unit. The antenna is designed on FR4 substrate with the inner diameter of 16.5 mm and the trace width of 7.8 mm. The gap between the two loops is 1.6 mm, which is equal to the height of the substrate. As shown in Fig. 4.18. (a), the 2-turn TX loop antenna of the on-body unit is placed 5 mm away from the skin. The 2-turn RX coil antenna of the in-body unit is placed in the CSF layer. The separation between the two antennas is 16 mm. The two inductively coupled loop antennas can be modeled as a two-port network and the maximum link power efficiency of the system can be calculated with Eq. (4.4). This link power efficiency is determined by the inherent electromagnetic properties of the system and the impedance matching is excluded. The power fed into the TX loop antenna should not exceed the $P_{t,max}$ that generates SAR_{max} (FCC regulation: 1.6 W/kg) in the closest tissue (skin, in this case). Since the SAR is proportional to the power delivered into the 2-turns loop antenna, the $P_{t,max}$ can be calculated with,

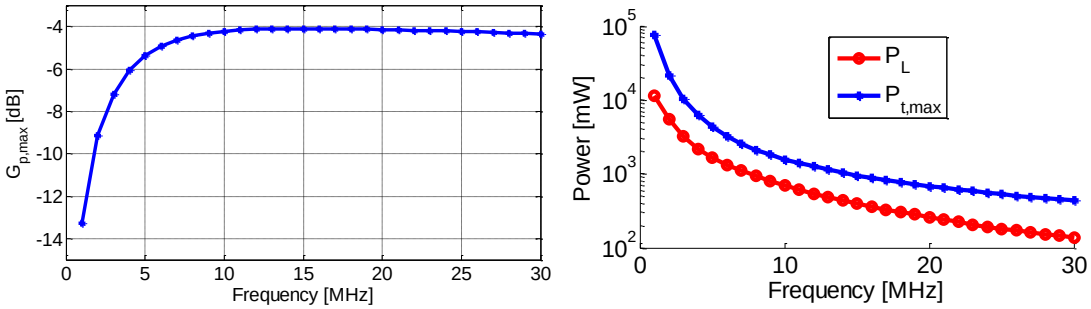

Fig. 4.19. (a) Link power efficiency ($G_{p,max}$) (b) maximum SAR-compliant transmission power ($P_{t,max}$) and power delivered to the implant antenna load (P_L) under conjugate-matched conditions

$$\frac{SAR}{\tau P_{test}} = \frac{SAR_{\max}}{P_{t,\max}}; \tau = \frac{4 \cdot 50\Omega \cdot \mathrm{Re}(Z_{ext})}{|50\Omega + Z_{ext}|^2}, \tag{4.10}$$

where P_{test} = 1 W is the power available from a 50 Ω test source in HFSS and τ is the power transfer efficiency between the test source and the 2-turns loop antenna (impedance: Z_{ext}). Hence, the maximum power available for a load connected to the coil antenna $P_L = P_{t,max}\, G_{p,max}$. Fig. 4.19. shows the simulated link power efficiency ($G_{p,max}$), maximum SAR-compliant transmission power ($P_{t,max}$) and power delivered to the implant antenna load (P_L) under conjugate-matched conditions. The simulation results shows that the maximum of $G_{p,max}$ of -4 dB occurs at 15 MHz. Fig. 4.20 shows the local SAR and

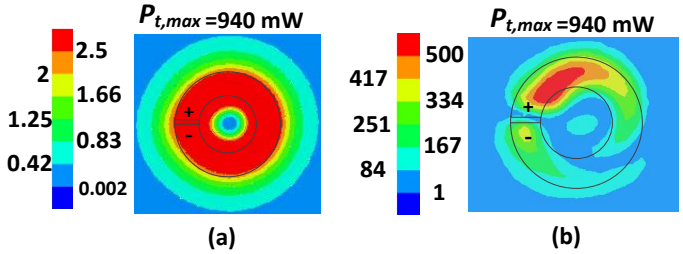

Fig. 4.20. (a) Local SAR (W/kg) distribution on the skin when maximum allowed power is transmitted at 15 MHz (b) Local E-field (V/m) distribution on the skin when maximum power is transmitted at 15 MHz

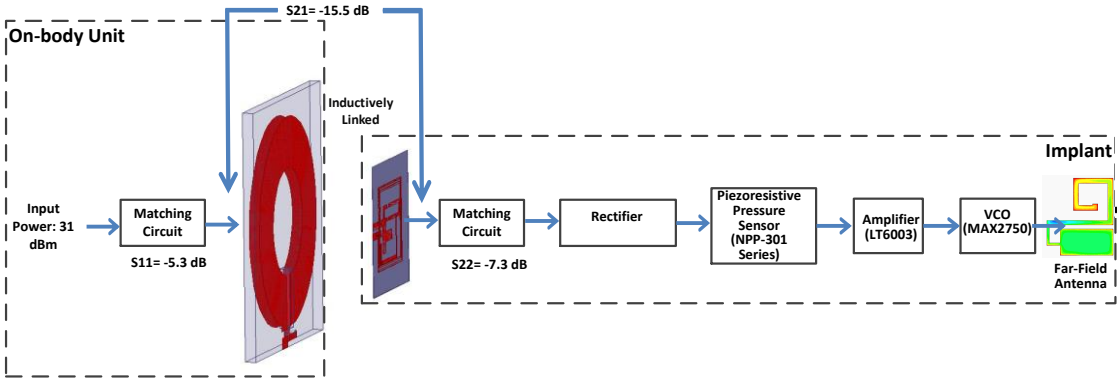

Fig. 4.21. Measured S-parameters and power transfer of wireless power transfer system.

the E-field distribution on the skin when $P_{t,max}$ of 940 mW is transmitted at 15 MHz. In the wireless measurement, the prototyped antennas were fabricated and tested in the tissue mimicking liquid. The port of the TX loop antenna was connected to the VNA port 1 and the RX coil antenna was connected to the VNA port 2. The two antennas were concentrically aligned with a separation distance of 16 mm. Fig. 4.21 shows the measured S-parameters and the power transferred. The measured transmission loss between the antennas is 15.5 dB. The reflection coefficients of the 2-turns loop antenna and 2-turns coil antenna are –5.3 dB and –7.3 dB respectively. With the input power of 31 dBm fed into the on-body unit and S11 of -5.3 dB, the power coupled to the on-body loop antenna is 889 mW which is under the maximum SAR-compliant transmission power $P_{t,max}$ (940 mW) at 15 MHz. The system power transfer efficiency is 2.81% and the power delivered to the rectifier is 13.17 dBm.

4.6 Far-field RFID Antennas for Intracranial Wireless Communication

In recent years, RFID technique, due to its favorable features such as the low power consumption and simple RF front-end structure, has been considered as a promising strategy in building the wireless data link for biomedical sensing applications. In [84], a tiny RFID sensor tag is proposed for continuous glucose monitoring. The authors of [85] developed the RFID sensor tag equipped with the helix antenna for wireless monitoring of drug dosage. In [86], an RFID based sensing platform is developed for continuous monitoring of the physiological data of animals. These RFID sensor tags harvest the energy from the reader's carrier wave and use impedance modulation to backscatter the data to the reader. Without the necessity of the battery and the active RF transmitter, the sensor size is significantly minimized. Since the operation of the RFID sensor tag entirely relies on the energy harvested from the incoming EM wave transmitted by the RFID reader, a proper impedance matching between the RFID IC and tag antenna becomes critical for the overall system performance. Unlike the most conventional antennas with a 50 Ohm resistance, the RFID antennas need to have an inductive impedance to obtain a proper complex conjugate matching to the RFID IC usually with a large capacitive reactance (for instance –100…–300 Ω) and a low resistance (for instance 20…50 Ω). In this subsection, we will introduce two techniques to develop the miniature implantable RFID antenna with high inductive antenna reactance for intracranial biomedical applications.

4.6.1 Split Ring Resonator Based Spatially Distributed Implantable Antenna System

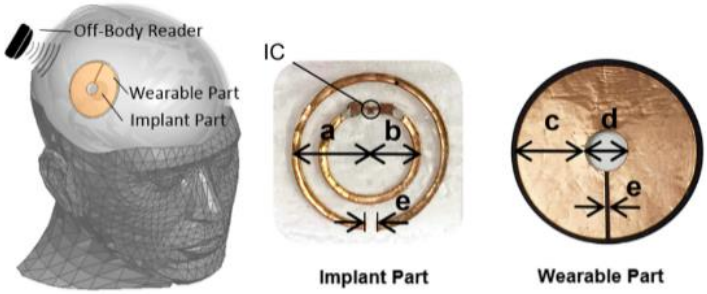

Geometrical parameter (mm)	a	b	c	d	e
	8.6	5.7	20.8	12.6	1.0

Fig. 4.22. Anatomical head model and antenna system with its geometrical dimensions.

Wireless electronic devices targeting for invasive biomedical applications need to meet the strict miniaturization requirement to minimize the invasiveness and reduce the risk of infections. This miniaturization requirement brings considerable challenge to the development of implantable antennas. Antennas with a miniaturized footprint inherently suffer from the low radiation efficiency and poor antenna directivity. When implanted in the lossy tissue environment, antenna RF performance becomes even worse. To obtain a proper antenna RF performance while maintain a small size of the implantable antenna, a spatially distributed implantable RFID antenna system is proposed in [67]. The proposed antenna system has a small implant part carrying the RFID microsystem and an inductively coupled wearable part for antenna gain improvement.

Fig. 4.22. demonstrates the antenna structure with its geometrical parameters and the implemented position in a layered ellipsoid model. The wearable part of the antenna system is attached on the scalp and the split ring resonator based implant part is concentrically implanted in the CSF tissue layer. The implant part is developed on the 50 µm thick flexible polyimide substrate (ε_r = 2.25, tanδ = 0.001 at 915 MHz) and the substrate for the wearable part is 2 mm thick EPDM (Ethylene-Propylene-Diene-Monomer; ε_r = 1.26, tanδ = 0.007 at 915 MHz). The NXP UCODE G2iL series RFID IC as the target microsystem was attached to the inner ring split of the implant part using the conductive epoxy - Circuit Works CW2400. The silicone coating (ε_r = 2.2, tanδ = 0.007 at 915 MHz) with a thickness of 1 mm is used to insulate the antenna from the tissue environment.

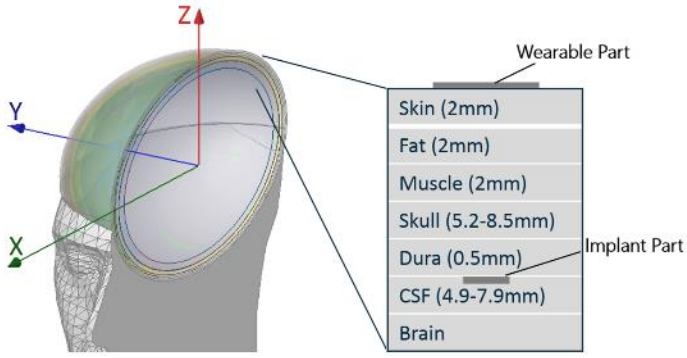

Fig. 4.23. Anatomical human head model with the layered ellipsoid.

The antenna simulation and optimization were conducted with the ANSYS High Frequency Structure Simulator (HFSS). In the simulation, the RFID IC is modeled as the parallel connection of the resistance and capacitance of 2.85 kΩ and 0.91 pF, respectively [87]. Meanwhile, the ANSYS anatomical human head model integrated with a seven-layer ellipsoid is built to mimic the human head. Fig. 4.23. shows the details of the anatomical head model combined with the layered ellipsoid. All the tissues were assigned with their corresponding relative permittivity and loss tangent according to the database of tissue dialectical properties from IT'IS Foundation [74].

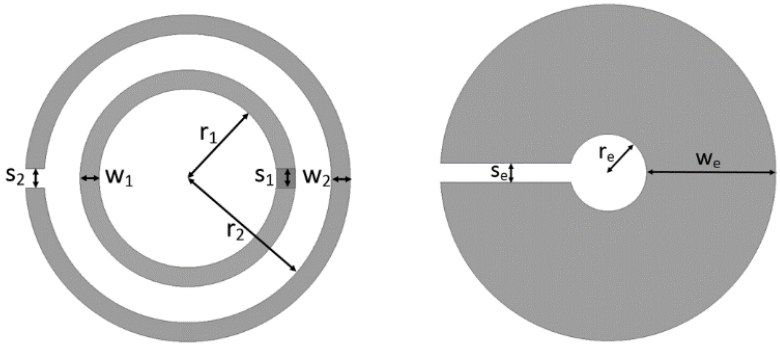

Fig. 4.24. Structure and dimension parameters of the antenna implantable part and wearable part

As shown in Fig. 4.24, the proposed antenna system has nine geometrical parameters. According to the parametric analysis conducted in [67], the antenna input impedance is dominated by the geometrical structure of the implant part and the wearable part only

influences the antenna directivity. To facilitate the process of antenna optimization, the geometrical parameters of the implant part is first determined. Then the dimension of the wearable part is optimized to maximize the antenna gain.

Among the six geometrical parameters of the implant part, the increase of the inner radius of the inner ring r_1 leads to the increase of the resistance and inductive reactance of the antenna input impedance. The inner radius of outer ring r_2, on the other hand, is proportional to the resistance of the antenna input impedance while reversely proportional to the inductive reactance of the antenna input impedance. Both the strip widths of the inner ring and outer ring has a reverse and positive relationship with the antenna resistance and inductive reactance, respectively. The increase of the rings' slit s_1 and s_2 will slightly decrease the antenna resistance, however it has negligible impact on antenna reactance. Overall, the inner radius of the inner ring r_1 is for coarse adjustment of the antenna input impedance and the rest of the parameters can be adjusted to achieve the good complex conjugate impedance matching to the RFID IC. For the NXP UCODE G2iL RFID IC that is modelled with the impedance of 20-j190 Ω at 915MHz, the optimal value of the r_1 and r_2 are 8.6 mm and 5.7 mm, respectively. Fig. 4.25. (a) compares the impedance of the antenna and the IC. A good impedance matching can be found near the 915 MHz. The corresponding power transfer efficacy defined by Eq. (4.8) is shown in Fig. 4.25. (b). The maximum power transfer efficiency reaches 70 % at 918 MHz.

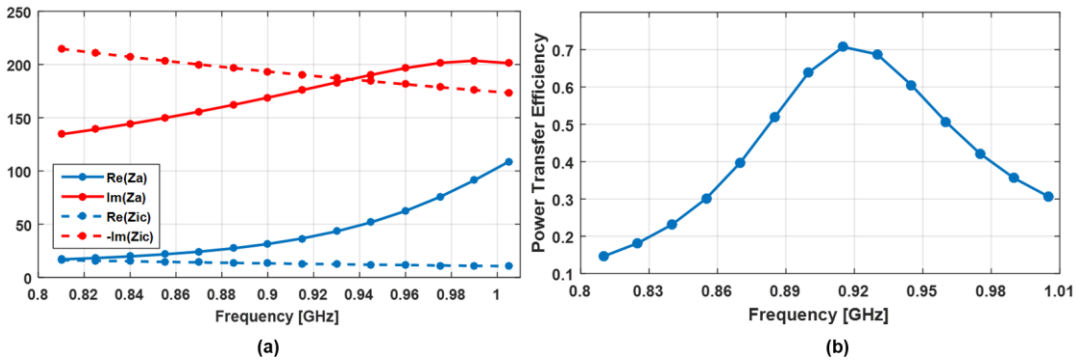

Fig. 4.25. (a) Antenna impedance and RFID IC impedance (b) Simulated power transfer efficiency

The implantable part alone has small directivity and low efficiency due to its small size and the lossy human tissue environment. The concentrically placed wearable part is proposed to improve the antenna gain in the far-field. As shown in Fig. 4.24, the wearable part has three geometrical parameters: the inner radius r_e, the strip width w_e and the width of the slit s_e. According to the simulation results, with the fixed dimension of the implant part, the three geometrical parameters of the wearable part have a parabolic correlation with the antenna directivity and radiation efficiency. The optimal values of r_e, w_e and s_e for maximizing the antenna gain are 6.3 mm, 20.8 mm and 1 mm, respectively. Finally, the wearable part provides more than 8 dB improvement to the antenna directivity (from -4.07dBi to 4.37dBi at 915MHz). Meanwhile, the simulated radiation efficiency is 0.48%. Fig. 4.26 (a) shows the radiation efficiency versus the frequency and the 3D radiation pattern at 915 MHz is shown in Fig. 4.26. (b). In the wireless measurement, the prototyped antenna system was evaluated with the Voyantic Tagformance measurement system in an anechoic chamber. Fig. 4.27 demonstrates the measurement setup. The head equivalent

liquid mixed with water, sugar and salt was used to mimic the human tissue environment. In the wireless measurement, the implant part was submerged in the liquid at three different implant depths: 5 mm, 10 mm and 15 mm. Fig. 4.28 shows the comparison between the measured read range and the simulated read ranges from the head model. A good match was found especially in 5 mm and 10 mm cases and the read range with 10 mm implant depth achieves 1.1 m.

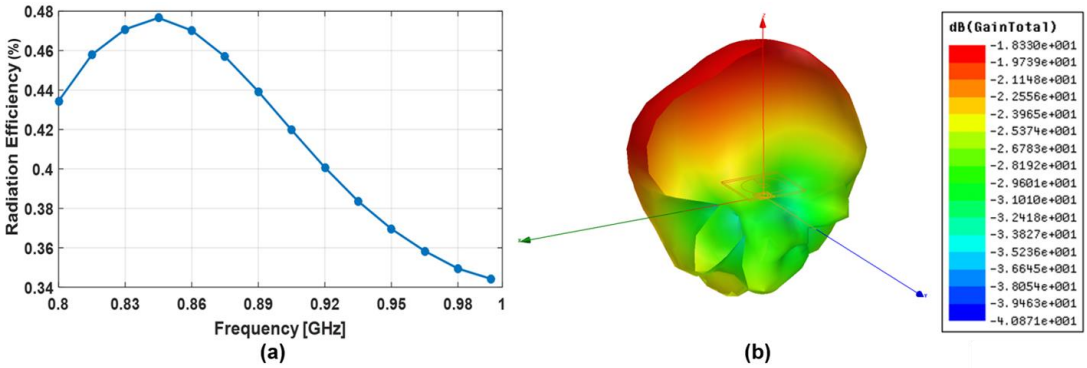

Fig. 4.26. (a) Antenna radiation efficiency (b) Simulated antenna 3D radiation pattern at 915 MHz

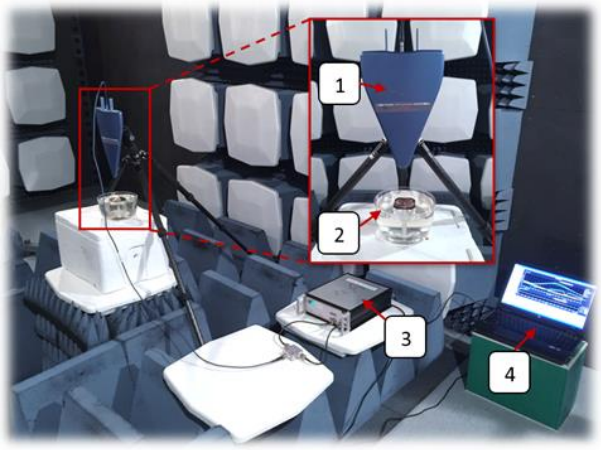

Fig. 4.27. Measurement setup 1: Reader antenna 2: Prototyped antenna system with the implantable part submerged in the liquid 3: Tagformance measurement unit 4: Tagformance software

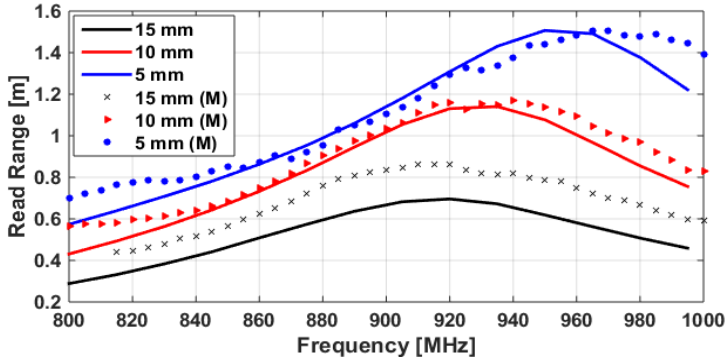

Fig. 4.28. Comparison of simulated and measured attainable read ranges in human-tissue-like liquid with different implant depths

4.6.2 LC-tank Based Miniature Implantable RFID Antenna

In [88], we proposed the design of an RFID antenna utilizing the coupled resonant LC-tank for antenna miniaturization. In the air, the size of the proposed antenna has been reduced to $0.04\lambda \times 0.04\lambda \times 0.02\lambda$ with a maximum read range of more 3 meters. In this subsection, we demonstrate the implementation of this LC-tank based RFID antenna for intracranial implantable applications. Fig. 4.29. shows the structure of the LC-tank based implantable RFID antenna with an anatomical head model. The proposed antenna is placed in the CSF layer with an implant depth of 16 mm.

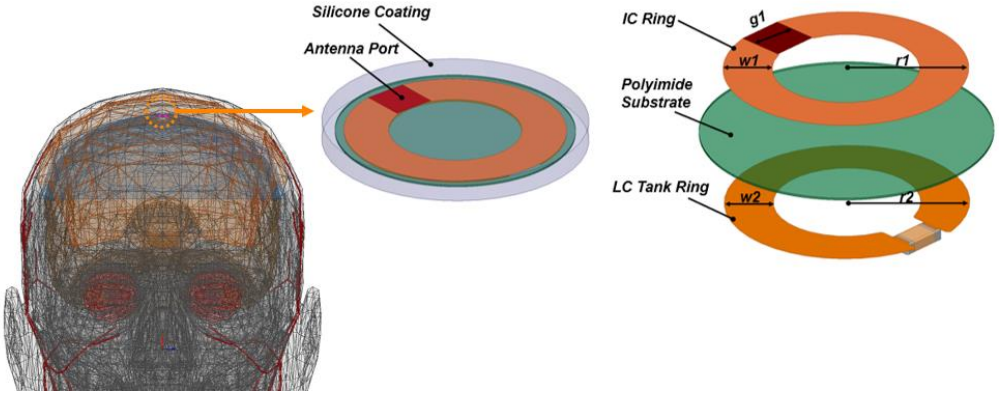

Fig. 4.29. Structure of the proposed antenna with the anatomical head model.

The antenna is composed of two concentric copper split rings (IC ring and LC tank ring) with an outer radius of r_1 and r_2, respectively. The antenna port is located at the terminals of the IC ring. The terminals of the LC tank ring are connected with a capacitor. The capacitance of the capacitor in series with the self-inductance from the copper ring together form the LC tank. The two rings are placed on the top and bottom sides of the 0.04 mm thick polyethylene (ε_r=2.25, tanδ=0.001 at 915 MHz), respectively. The insulation material used in this work is 0.5 mm thick silicone (ε_r=2.2, tanδ=0.007 at 915 MHz).

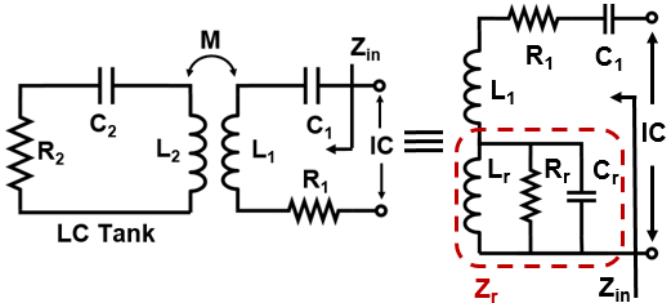

Fig. 4.30. Equivalent circuit of the proposed antenna.

The inductive coupling between the two loops can be analyzed with the equivalent circuit model shown in Fig. 4.30., where L_1, C_1 and R_1 are the inductance, parasitic capacitance and parasitic resistance of the IC ring, respectively. L_2, C_2 and R_2 are the inductance, capacitance of the paralleled lumped capacitor and parasitic capacitance and the parasitic

resistance of the LC tank ring. The M stands for the mutual inductance between the two rings. The input impedance from the IC port, Z_{in} can be calculated using the reflected load theory [89] as,

$$Z_{in} = R_1 + j\omega L_1 + \frac{1}{j\omega C_1} + Z_r \tag{4.11}$$

$$where, Z_r = \frac{\omega^2 M^2}{j\omega L_2 + \frac{1}{j\omega C_2} + R_2}. \tag{4.12}$$

According to Eq. (4.11), the antenna input impedance is not only related to L_1, C_1 and R_1 from the IC ring but also influenced by L_2, C_2 and R_2 of the LC tank ring as well as the mutual inductance M. All of these parameters, except the capacitance from the lumped capacitor, are determined by the geometrical structure of the antenna system. To find out the relationship between the antenna structure and the attainable input impedance of the proposed antenna, we built the antenna model in the ANSYS High Frequency Structure Simulator and conducted the parametric analysis. In the simulation, the HFSS anatomical head model is adopted to simulate the human head. There are in total six parameters evaluated in the analysis including the capacitance of the lumped capacitor and five geometrical parameters of the antenna which are the outer radius of the two rings r_1 and r_2, trace width of the two rings w_1 and w_2 and the split gap width g_1 of the IC ring. Based on the results of the parametric analysis, the g_1 is found to have negligible effect on the antenna input impedance. On the contrary, the difference between the r_1 and r_2 and the capacitance of the lumped capacitor have the dominant influence on the antenna input impedance. Keeping in mind the antenna miniaturization, we fixed the r_1 to 3 mm and gradually increase the r_2 from 3 mm to 5 mm with a step of 0.25 mm. In each combination of r_1 an r_2, the capacitance of the lumped capacitor sweeped from 0.5 pF to 4 pF with a step of 0.1 pF. In this study, the w_1 and w_2 were set to 1 mm.

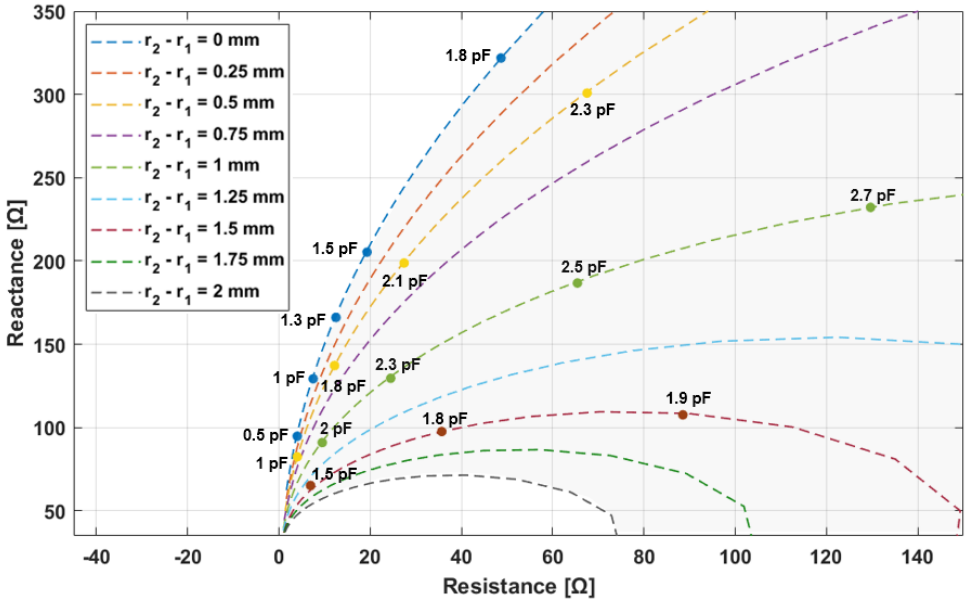

Fig. 4.31. Simulated range of the attainable antenna input impedance.

Fig. 4.31 plots the results of the parametric analysis. In Fig. 4.31, each dash line with different colors indicates the impedance value with certain r_2-r_1. Obviously, both resistance and the reactance of the antenna input impedance is reversely proportional to the increase of the r_2-r_1. When the r_2-r_1 is fixed to a certain value, the antenna input impedance can be further adjusted by changing the capacitance of the lumped capacitor. For instance, the deep blue line represents the range of the antenna input impedance when the r_2 and r_1 are equal to 3 mm. By increasing the capacitance of the lumped capacitor, the antenna input impedance increases along this line. Theoretically, the shadowed area in Fig. 4.31 is the range of the attainable antenna input impedance at 915 MHz with difference combination of the r_1, r_2 and the capacitance of the capacitor. This range covers the typical impedance values to achieve the complex conjugate matching to a majority of the RFID ICs.

In this study, we chose the NXP UCODE G2iL series RFID IC as the target microsystem for antenna evaluation and the wireless measurement. This IC has the impedance of 20-j190 Ω at 915MHz with a wake-up power threshold of -18 dBm. In the simulation, the RFID IC was modeled as the parallel connection of the resistance and capacitance of 2.85 kΩ and 0.91 pF, respectively. The HFSS optimization tool was used to determine the antenna geometrical parameters that optimize the complex conjugate matching to the IC. Fig. 4.31. (a) compares the impedance of the IC and the antenna with the r_1, r_2, w_1 and w_2 equal to 3 mm, 3.2 mm, 1 mm and 1mm, respectively and the capacitance of the capacitor is 1.5 pF. A good matching can be observed in Fig. 4.32. (b). At 915 MHz, the corresponding power reflection coefficient reaches -12.4 dB.

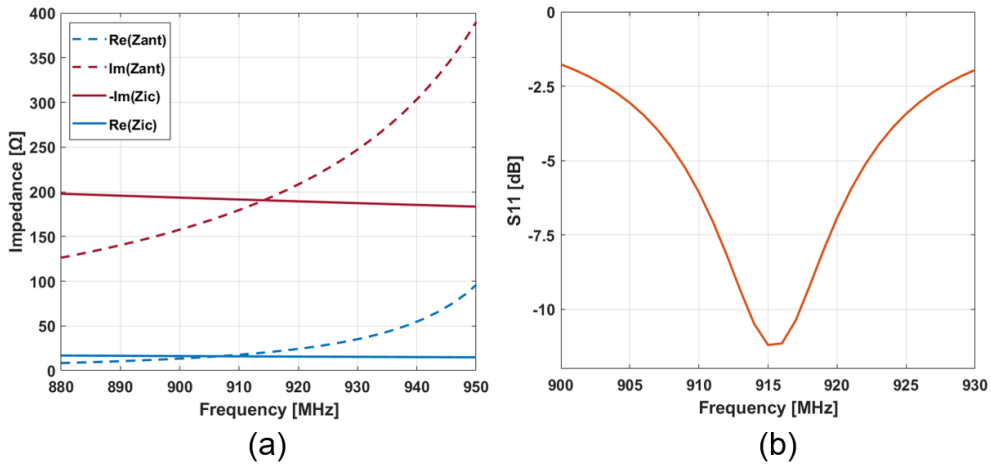

Fig. 4.32. (a) Comparison of the simulated antenna impedance and the IC impedance (b) Simulated antenna power reflection coefficient

Fig. 4.33. (a) shows the antenna far-field radiation pattern in E plane and H plane when implemented in the intracranial environment. The proposed antenna has a maximum directivity of 3.6 dBi with a direction outwards the human head. Fig. 4.33. (b) shows the 3D radiation pattern of the antenna gain with the maximum value of -34.2 dBi.

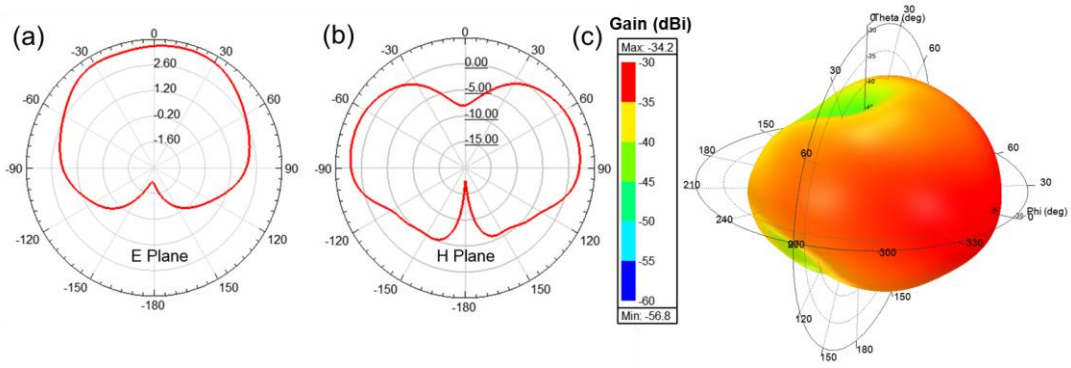

Fig. 4.33. (a) Antenna radiation pattern in E plane (b) Antenna radiation pattern in H plane (c) 3D radiation pattern of the proposed antenna

Antenna Prototype and Wireless Measurement

To evaluate the antenna performance in a realistic tissue environment, we made the prototype and conducted the wireless measurement with the tissue mimicking liquid and in-vivo test in the head of a rat. The antenna was first evaluated in a tissue box model with the size (50 mm × 50 mm × 50 mm) comparable to the dimension of the mouse head. This tissue box was assigned with the dielectric properties of the "averaged head" provided by the FCC. In the simulation, the proposed antenna maintains a good complex conjugate matching with the IC at 915 MHz. While, the antenna gain, due to the reduced dimensions of the tissue box compared with the human head model, improved to -15.4 dBi. Then, the prototyped antenna was evaluated with the tissue mimicking liquid with the relative permittivity of 45.74 and conductivity 0.77 S/m at 915 MHz.

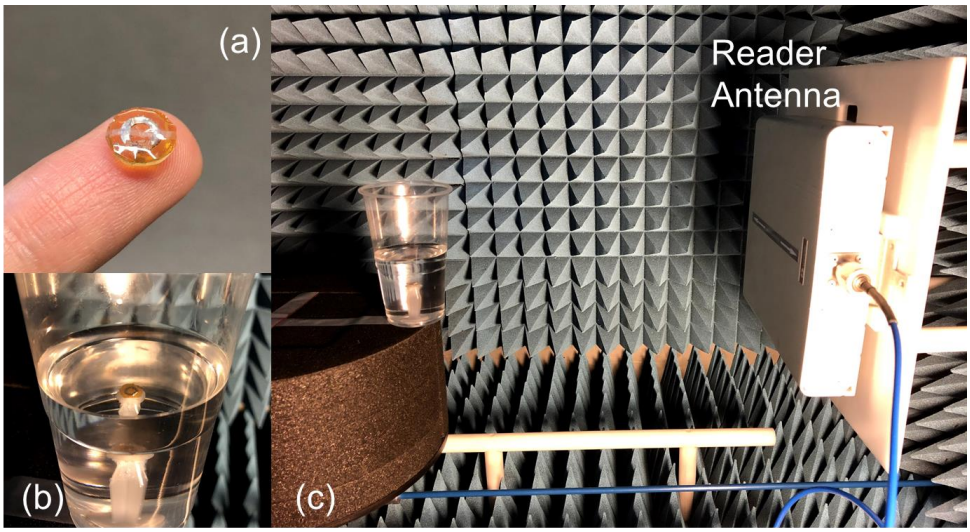

Fig. 4.34. (a) Prototyped Antenna (b) Prototyped antenna with the tissue mimicking liquid (c) Setup for the wireless measurement with the tissue mimicking liquid.

Fig. 4.34 (a) shows the fabricated antenna with the silicone coating wrapping the two split rings and the polyimide substrate. The RFID IC and the ceramic capacitor were soldered to the terminals of the upper ring and lower ring, respectively. The measurement setup is shown in Fig. 4.34 (b) and (c) where the antenna was immersed inside the liquid and the Voyantic Tagformance RFID evaluation system with a linear polarized patching reader antenna was used to read the response from the IC.

Followed the evaluation with the liquid, an in-vivo test was conducted with a rat. Fig. 4.35 (a) demonstrates the implementation of the antenna inside the rat cranial cavity. The antenna was implanted under the rat skull with an implant depth around 6 mm. Fig. 4.35. (b) demonstrates the measurement setup for the in-vivo test. The distance between the reader antenna and the rat with the implanted antenna is 30 cm.

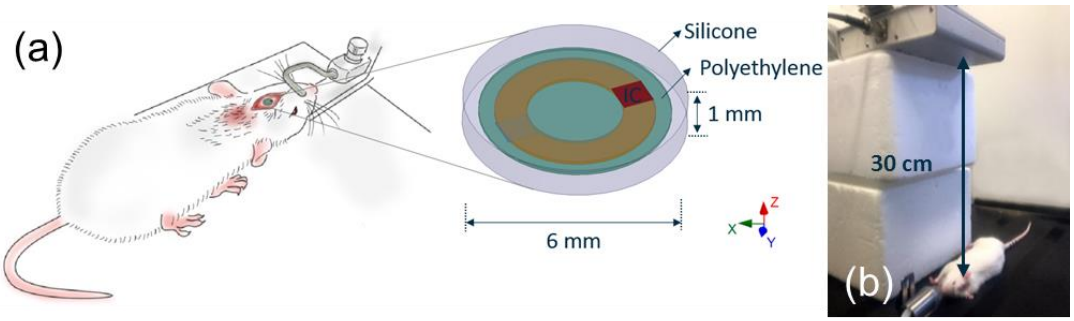

Fig. 4.35. (a) Implementation of the proposed antenna in rat head (b) Measurement setup for the in-vivo test.

Fig. 4.36. compares the read ranges of the wireless measurement in the tissue mimicking liquid, the in-vivo test with the rat and the simulation with the tissue box model. The result from the in-vivo test has a good agreement with that from the liquid test and better performance than that in the simulation. According to the red line in Fig. 4.36, the estimated maximum attainable read range of the proposed antenna reaches 1 m when implanted 6 mm in the rat's cranial cavity.

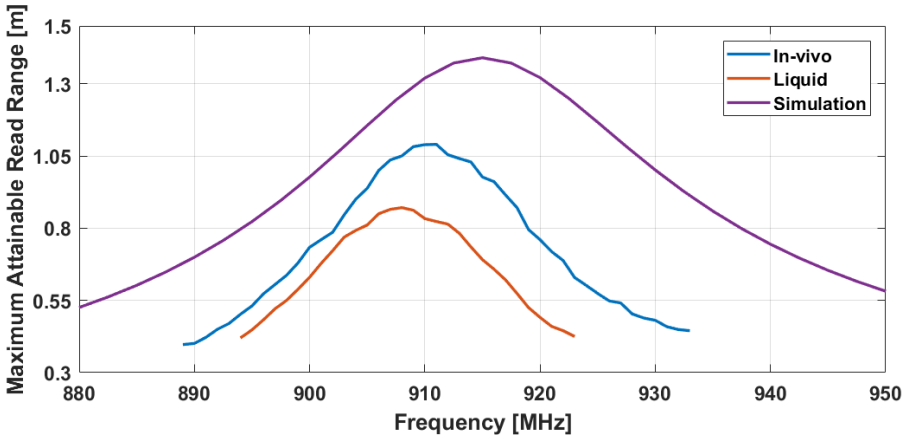

Fig. 4.36. The measured and simulated read range of the prototyped antenna.

4.7 Conclusion

Wireless intracranial implantable devices are believed to potentially innovate the management of brain disorders and the treatment of neurological diseases. Over the past few years, various implantable antennas and wireless power transfer techniques have been proposed to establish the wireless through-body radio link for biomedical applications. In this chapter, we briefly discussed the challenges in developing the intracranial implantable antennas and compared different techniques for wireless power transfer in the presence of human body tissues. A brief summary of the most recent miniature implantable antennas and inductive power transfer systems for implantable applications is provided, respectively. Next, we discussed and compared the merits of different methodologies to build the computational head models for implantable antenna development. A thorough comparison of the human head models with different complexity is provided. Then, the development and the performance of a wirelessly powered intracranial pressure sensing system integrating near- and far field antennas were elaborately discussed in the human head environment. Additionally, two far-field RFID antennas for intracranial wireless communication were demonstrated and evaluated. The antenna performance and the tuning parameters were discussed through a parametric analysis.

Reference

[1] Zago, Stefano et al. "Bartholow, Sciamanna, Alberti: Pioneers in the Electrical Stimulation of the Exposed Human Cerebral Cortex," *History of Neuroscience*, 2008.

[2] Lebedev, Mikhail A. and Miguel A. L. Nicolelis. "Brain–machine interfaces: past, present and future," *Trends in Neurosciences* 29 (2006): 536-546.

[3] Chapin, J.K .et al.(1999) "Real-time control of a robot arm using simultaneously recorded neurons in the motor cortex," *Nat.Neurosci*.2, 664–670

[4] Nicolelis, M. "Actions from thoughts," *Nature* 409, 403–407, 2001.

[5] Flora, E.D., Perera, C.L., Cameron, A.L. and Maddern, G.J. "Deep brain stimulation for essential tremor: A systematic review," *Mov. Disord.*, 25: 1550-1559, 2010.

[6] M. A. Shaeri and A. M. Sodagar, "A Method for Compression of Intra-Cortically-Recorded Neural Signals Dedicated to Implantable Brain–Machine Interfaces," *IEEE Transactions on Neural Systems and Rehabilitation Engineering*, vol. 23, no. 3, pp. 485-497, May 2015.

[7] Pazzini, L., Polese, D., Weinert, J.F. et al. "An ultra-compact integrated system for brain activity recording and stimulation validated over cortical slow oscillations in vivo and in vitro," *Sci. Rep. 8*, 16717, 2018

[8] Chen, R., Canales, A. & Anikeeva, P. "Neural recording and modulation technologies," *Nat. Rev. Mater* 2, 16093, 2017

[9] M. W. A. Khan, M. Rizwan et al, Y. Rahmat-Samii and L. Ukkonen, "Characterization of 3-D Loop Antenna to Overcome the Impact of Small Lateral Misalignment in Wirelessly Powered Intracranial Pressure Monitoring System," *IEEE Transactions on Antennas and Propagation*, vol. 65, no. 12, pp. 7405-7410, Dec. 2017.

[10] J. Wang, H. Xie, T. Chung, L. L. H. Chan, and S. W. Pang, "Neural probes with integrated temperature sensors for monitoring retina and brain implantation and

stimulation," *IEEE Trans. Neural Syst. Rehabil. Eng.*, vol. 25, no. 9, pp. 1663–1673, Sep. 2017.
[11] C. W. Lee, A. Kiourti, J. Chae, and J. L. Volakis, "A high-sensitivity fully passive neurosensing system for wireless brain signal monitoring," *IEEE Trans. Microw. Theory Techn.*, vol. 63, no. 6, pp. 2060–2068, Jun. 2015.
[12] C. Pena et al., "An Overview of FDA Medical Device Regulation as it Relates to Deep Brain Stimulation Devices," *IEEE Transactions on Neural Systems and Rehabilitation Engineering*, vol. 15, no. 3, pp. 421-424, Sept. 2007.
[13] C. O. Oluigbo, A. Salma and A. R. Rezai, "Deep Brain Stimulation for Neurological Disorders," *IEEE Reviews in Biomedical Engineering*, vol. 5, pp. 88-99, 2012.
[14] A. Mohammed, M. Zamani, R. Bayford and A. Demosthenous, "Toward On-Demand Deep Brain Stimulation Using Online Parkinson's Disease Prediction Driven by Dynamic Detection," *IEEE Transactions on Neural Systems and Rehabilitation Engineering*, vol. 25, no. 12, pp. 2441-2452, Dec. 2017.
[15] H. Kim, H. Hirayama, S. Kim, K. J. Han, R. Zhang and J. Choi, "Review of Near-Field Wireless Power and Communication for Biomedical Applications," *IEEE Access*, vol. 5, pp. 21264-21285, 2017.
[16] Zeng FG, Rebscher S, Harrison W, Sun X, Feng H. "Cochlear implants: system design, integration, and evaluation," *IEEE Rev Biomed Eng*. 2008.
[17] Hendry, M.. *Near Field Communications Technology and Applications*. Cambridge: Cambridge University Press, 2014.
[18] Y. Zhang, C. Liu, X. Liu, K. Zhang and X. Yang, "A Wideband Circularly Polarized Implantable Antenna for 915 MHz ISM-Band Biotelemetry Devices," *IEEE Antennas and Wireless Propagation Letters*, vol. 17, no. 8, pp. 1473-1477, Aug. 2018.
[19] S. Das and D. Mitra, "A Compact Wideband Flexible Implantable Slot Antenna Design With Enhanced Gain," *IEEE Transactions on Antennas and Propagation*, vol. 66, no. 8, pp. 4309-4314, Aug. 2018.
[20] Z. Chen, H. Sun and W. Geyi, "Maximum Wireless Power Transfer to the Implantable Device in the Radiative Near Field," *IEEE Antennas and Wireless Propagation Letters*, vol. 16, pp. 1780-1783, 2017.
[21] X. Y. Liu, Z. T. Wu, Y. Fan and E. M. Tentzeris, "A Miniaturized CSRR Loaded Wide-Beamwidth Circularly Polarized Implantable Antenna for Subcutaneous Real-Time Glucose Monitoring," *IEEE Antennas and Wireless Propagation Letters*, vol. 16, pp. 577-580, 2017.
[22] B. Rana, J. Shim and J. Chung, "An Implantable Antenna With Broadside Radiation for a Brain–Machine Interface," *IEEE Sensors Journal*, vol. 19, no. 20, pp. 9200-9205, 15 Oct.15, 2019.
[23] S. A. A. Shah and H. Yoo, "Scalp-Implantable Antenna Systems for Intracranial Pressure Monitoring," *IEEE Transactions on Antennas and Propagation*, vol. 66, no. 4, pp. 2170-2173, April 2018.
[24] A. Abdi and H. Aliakbarian, "A Miniaturized UHF-Band Rectenna for Power Transmission to Deep-Body Implantable Devices," *IEEE Journal of Translational Engineering in Health and Medicine*, vol. 7, pp. 1-11, 2019
[25] M. Manoufali, K. Bialkowski, B. Mohammed, P. C. Mills and A. M. Abbosh, "Compact Implantable Antennas for Cerebrospinal Fluid Monitoring," *IEEE Transactions on Antennas and Propagation*, vol. 67, no. 8, pp. 4955-4967, Aug. 2019.

[26] A. Sharma, E. Kampianakis and M. S. Reynolds, "A Dual-Band HF and UHF Antenna System for Implanted Neural Recording and Stimulation Devices," *IEEE Antennas and Wireless Propagation Letters*, vol. 16, pp. 493-496, 2017.
[27] Z. Jiang et al., "Wideband Loop Antenna With Split-Ring Resonators for Wireless Medical Telemetry," *IEEE Antennas and Wireless Propagation Letters*, vol. 18, no. 7, pp. 1415-1419, July 2019.
[28] J. M. Elloian, G. M. Noetscher, S. N. Makarov, A. Pascual-Leone, "Continuous wave simulations on the propagation of electromagnetic fields through the human head," *IEEE Trans. Biomed. Eng.*, vol. 61, no. 6, pp. 1676-1683, 2014.
[29] R. E. Collin, F. J. Zucker, *Antenna Theory*, New York, NY, USA: McGraw-Hill, 1969.
[30] R. V. Taalla, M. S. Arefin, A. Kaynak and A. Z. Kouzani, "A Review on Miniaturized Ultrasonic Wireless Power Transfer to Implantable Medical Devices," *IEEE Access*, vol. 7, pp. 2092-2106, 2019.
[31] F. Mazzilli, C. Lafon, and C. Dehollain, "A 10.5 cm ultrasound link for deep implanted medical devices," *IEEE Trans. Biomed. Circuits Syst*., vol. 8, no. 5, pp. 738–750, 2014.
[32] William R. Hendee. *Medical Imaging Physics*, Fourth Edition. Wiley-Liss, 2002.
[33] A. G. Fowler and S. O. R. Moheimani, "A 4-DOF MEMS Energy Harvester Using Ultrasonic Excitation," *IEEE Sensors Journal*, vol. 16, no. 21, pp. 7774-7783, Nov.1, 2016.
[34] H. Kawanabe, T. Katane, H. Saotome, O. Saito, and K. Kobayashi, "Power and Information Transmission to Implanted Medical Device Using Ultrasonic," *Jpn. J. Appl. Phys.*, vol. 40, no. 5, 2001.
[35] M. Zargham and P. G. Gulak, "Maximum Achievable Efficiency in Near-Field Coupled Power-Transfer Systems," *IEEE Trans. Biomed. Circuits Syst.*, vol. 6, no. 3, pp. 228-245, June 2012.
[36] D. C. Galbraith, "An implantable multichannel neural stimulator," Ph.D. dissertation, Elect. Eng., Stanford Univ., Stanford, CA, USA, Dec. 1984.
[37] W. J. Heetderks, "RF powering of millimeter- and submillimeter-sized neural prosthetic implants," *IEEE Trans. Biomed. Eng.*, vol. 35, no. 5, pp. 323–327, May 1988.
[38] M. Schormans, V. Valente and A. Demosthenous, "Practical Inductive Link Design for Biomedical Wireless Power Transfer: A Tutorial," *IEEE Trans. Biomed. Circuits Syst.*, vol. 12, no. 5, pp. 1112-1130, Oct. 2018.
[39] F. C. Flack, E. D. James, and D. M. Schlapp, "Mutual inductance of air-cored coils: Effect on design of radio-frequency coupled implants," *Med. Biol. Eng.*, vol. 9, no. 2, pp. 79–85, Mar. 1971.
[40] W. H. Ko, S. P. Liang, and C. D. Fung, "Design of radio-frequency powered coils for implant instruments," *Med. Biol. Eng. Comput.*, vol. 15, pp. 634–640, 1977.
[41] M. Soma, D. C. Galbraith and R. L. White, "Radio-Frequency Coils in Implantable Devices: Misalignment Analysis and Design Procedure," *IEEE Trans. Biomed. Eng.*, vol. BME-34, no. 4, pp. 276-282, April 1987.
[42] U. Jow and M. Ghovanloo, "Design and Optimization of Printed Spiral Coils for Efficient Transcutaneous Inductive Power Transmission," *IEEE Trans. Biomed. Circuits Syst.*, vol. 1, no. 3, pp. 193-202, Sept. 2007.

[43] D. Jiang, D. Cirmirakis, M. Schormans, T. A. Perkins, N. Donaldson, A. Demosthenous, "An integrated passive phase-shift keying modulator for biomedical implants with power telemetry over a single inductive link," *IEEE Trans. Biomed. Circuits Syst.*, vol. 11, no. 1, pp. 64-77, Feb 2017.
[44] S. A. Mirbozorgi, P. Yeon, M. Ghovanloo, "Robust wireless power transmission to mm-sized free-floating distributed implants," *IEEE Trans. Biomed. Circuits Syst.*, vol. 11, no. 3, pp. 692-702, Jun 2017.
[45] N. Soltani, M. S. Aliroteh, M. T. Salam, J. L. P. Velazquez, and R. Genov, "Low-radiation cellular inductive powering of rodent wireless brain interfaces: Methodology and design guide," *IEEE Trans. Biomed. Circuits Syst.*, vol. 10, no. 4, pp. 920–932, Aug. 2016.
[46] Q. Xu, D. Hu, B. Duan, and J. He, "A fully implantable stimulator with wireless power and data transmission for experimental investigation of epidural spinal cord stimulation," *IEEE Trans. Neural Syst. Rehabil. Eng.*, vol. 23, no. 4, pp. 683–692, Jul. 2015.
[47] A. Ibrahim and M. Kiani, "A figure-of-merit for design and optimization of inductive power transmission links for millimeter-sized biomedical implants," *IEEE Trans. Biomed. Circuits Syst.*, vol. 10, no. 6, pp. 1100–1111, Dec. 2016.
[48] D. Ahn and M. Ghovanloo, "Optimal design of wireless power transmission links for millimeter-sized biomedical implants," *IEEE Trans. Biomed. Circuits Syst.*, vol. 10, no. 1, pp. 125–137, Feb. 2016.
[49] M. Manoufali, K. Bialkowski, B. Mohammed and A. Abbosh, "Wireless Power Link Based on Inductive Coupling for Brain Implantable Medical Devices," *IEEE Antennas and Wireless Propagation Letters*, vol. 17, no. 1, pp. 160-163, Jan. 2018.
[50] Ho JS, Yeh AJ, Neofytou E, et al., "Wireless power transfer to deep-tissue microimplant," in *Proc. Natl. Acad. Sci.* U S A. 2014
[51] A. Aldaoud et al., "Near-Field Wireless Power Transfer to Stent-Based Biomedical Implants," *IEEE Journal of Electromagnetics, RF and Microwaves in Medicine and Biology*, vol. 2, no. 3, pp. 193-200, Sept. 2018.
[52] E. Moradi, L. Sydänheimo, G. S. Bova and L. Ukkonen, "Measurement of Wireless Power Transfer to Deep-Tissue RFID-Based Implants Using Wireless Repeater Node," *IEEE Antennas and Wireless Propagation Letters*, vol. 16, pp. 2171-2174, 2017.
[53] M. Machnoor, E. S. Gámez Rodríguez, P. Kosta, J. Stang and G. Lazzi, "Analysis and Design of a 3-Coil Wireless Power Transmission System for Biomedical Applications," *IEEE Trans. Antennas Propag.*, vol. 67, no. 8, pp. 5012-5024, Aug. 2019.
[54] K., W., Jia, Y., Madi, F. et al. "Inductively coupled, mm-sized, single channel optical neuro-stimulator with intensity enhancer," *Microsyst. Nanoeng* 5, 23, 2019.
[55] A. S. Y. Poon, S. O'Driscoll, and T. H. Meng, "Optimal frequency for wireless power transmission over dispersive tissue," *IEEE Trans. Antennas Propag.*, vol. 58, no. 5, pp. 1739–1749, May 2010.
[56] A. M. Niknejad, *Electromagnetics for High-Speed Analog and Digital Communication Circuits*, Cambridge University Press, 2007.
[57] R. S. Carson, *High-frequency amplifiers*, Wiley, 1982.
[58] Pozar, David M. *Microwave Engineering*. Hoboken, Wiley, 2012.

[59] E. Moradi *et al*., "Backscattering Neural Tags for Wireless Brain-Machine Interface Systems," *IEEE Trans. Antennas Propag.*, vol. 63, no. 2, pp. 719-726, Feb. 2015.
[60] J. M. Rabaey *et al*., "Powering and communicating with mm-size implants," in *2011 Design, Automation & Test in Europe*, Grenoble, 2011, pp. 1-6.
[61] M. W. A. Khan, L. Sydänheimo, L. Ukkonen and T. Björninen, "Inductively Powered Pressure Sensing System Integrating a Far-Field Data Transmitter for Monitoring of Intracranial Pressure," *IEEE Sensors Journal*, vol. 17, no. 7, pp. 2191-2197, 1 April1, 2017.
[62] T. Björninen, "Extrema of transducer power gain and voltage gain of two-port network under varying terminations: semi-analytical method and application to biotelemetry system," *Appl. Computational Electromagn. Soc. J.*, vol. 33, no. 6, pp. 561–568, June 2018.
[63] J. Kim and Y. Rahmat-Samii, "Implanted antennas inside a human body: simulations, designs, and characterizations," *IEEE Transactions on Microwave Theory and Techniques*, vol. 52, no. 8, pp. 1934-1943, Aug. 2004.
[64] A. Kiourti and K. S. Nikita, "A Review of Implantable Patch Antennas for Biomedical Telemetry: Challenges and Solutions [Wireless Corner]," *IEEE Antennas and Propagation Magazine*, vol. 54, no. 3, pp. 210-228, June 2012.
[65] S. N. Makarov et al., "Virtual Human Models for Electromagnetic Studies and Their Applications," *IEEE Reviews in Biomedical Engineering*, vol. 10, pp. 95-121, 2017.
[66] T. S. P. See, X. Qing, W. Liu and Z. N. Chen, "A Wideband Ultra-Thin Differential Loop-Fed Patch Antenna for Head Implants," *IEEE Trans. Antennas Propag.*, vol. 63, no. 7, pp. 3244-3248, July 2015.
[67] S. Ma, L. Sydänheimo, L. Ukkonen and T. Björninen, "Split-Ring Resonator Antenna System With Cortical Implant and Head-Worn Parts for Effective Far-Field Implant Communications," *IEEE Antennas and Wireless Propagation Letters*, vol. 17, no. 4, pp. 710-713, April 2018.
[68] B. Rana, J. Shim and J. Chung, "An Implantable Antenna With Broadside Radiation for a Brain–Machine Interface," IEEE Sensors Journal, vol. 19, no. 20, pp. 9200-9205, 15 Oct.15, 2019.Implant Communication for Future Leadless Cardiac Pacemakers," *IEEE Transactions on Biomedical Engineering*, vol. 65, no. 12, pp. 2798-2807, Dec. 2018.
[69] L. Song and Y. Rahmat-Samii, "An End-to-End Implanted Brain–Machine Interface Antenna System Performance Characterizations and Development," *IEEE Trans. Antennas Propag.*, vol. 65, no. 7, pp. 3399-3408, July 2017.
[70] A. Sharma, E. Kampianakis and M. S. Reynolds, "A Dual-Band HF and UHF Antenna System for Implanted Neural Recording and Stimulation Devices," *IEEE Antennas and Wireless Propagation Letters*, vol. 16, pp. 493-496, 2017.
[71] J. Yanamadala et al., "New VHP-female V.2.0 full-body computational phantom and its performance metrics using FEM simulator ANSYS HFSS," in *Proc. 37th Annu. Int. Conf. IEEE Eng. Med. Biol. Soc.*, Milano, Italy, pp. 3237–3241, Aug. 2015.
[72] G. M. Noetscher, A. T. Htet, N. Maino, and P. Lacroix, "The visible human project male CAD based computational phantom and its use in bioelectromagnetic simulations," in *Proc. 39th Annu. Int. Conf. IEEE Eng. Med. Biol. Soc.*, Jeju Island, South Korea, Jul. 11–15, 2017.

[73] C. Wenger, R. Salvador, P. J. Basser, and P. C. Miranda, "The electric field distribution in the brain during TTFields therapy and its dependence on tissue dielectric properties and anatomy: A computational study," *Phys. Med. Biol.*, vol. 60, no. 18, pp. 7339–7357, Sep. 2015.
[74] P. A. Hasgall et al., "IT'IS database for thermal and electromagnetic parameters of biological tissues," Version 3.0, Sep. 2015. [Online]. Available: www.itis.ethz.ch/database
[75] S. Gabriel, R. W. Lau, and C. Gabriel, "The dielectric properties of biological tissues: II. Measurements in the frequency range 10Hz to 20 GHz," *Phys. Med. Biol.*, vol. 41, no. 11, pp. 2251–2269, Nov. 1996.
[76] S. Gabriel, R. W. Lau, and C. Gabriel, "The dielectric properties of biological tissues: Part III. Parametric models for the dielectric spectrum of tissues," *Phys. Med. Biol.*, vol. 41, no. 11, pp. 2271–2293, Nov. 1996.
[77] P. H. Raboel, J. Bartek Jr., M. Andresen, B. M. Bellander, B. Romner, "Intracranial pressure monitoring: invasive versus non-invasive methods – a review," *Crit. Care Res. Pract.*, vol. 2012, article ID: 950393, Mar. 2012.
[78] U. Kawoos, M.-R. Tofighi, R. Warty, F. A. Kralick, A. Rosen, "In-vitro and in-vivo trans-scalp evaluation of an intracranial pressure implant at 2.4 GHz," *IEEE Trans. Microw. Theory Techn.*, nol. 56, no. 10, pp. 2356–2365, Oct. 2008.
[79] P. Hu, Y. W. You, F. Y. B. Chen, D. McCormick, D. M. Budgett, "Wireless power supply for ICP devices with hybrid supercapacitor and battery storage," *IEEE J. Emerg. Sel. Topics Power Electron.*, vol. 4, no. 1, pp. 273–279, Mar. 2016.
[80] L. Y. Chen, B. C. K. Tee, Z. Bao, et al., "Continuous wireless pressure monitoring and mapping with ultra-small passive sensors for health monitoring and critical care," *Nature Commun.*, vol. 5, article 5028, Oct. 2014.
[81] M. H. Behfar, E. Moradi, T. Björninen, L. Sydänheimo, L. Ukkonen, "Biotelemetric wireless intracranial pressure monitoring: an in vitro study," *Intl. J. Antennas and Propag.*, vol. 2015, article ID 918698, 10 pages, Nov. 2015.
[82] M. W. A. Khan, L. Sydänheimo, L. Ukkonen, T. Björninen, "Inductively powered pressure sensing system integrating a far-field data transmitter for monitoring of intracranial pressure," *IEEE Sensors J.*, vol. 17, no. 7, pp. 2191–2197, Apr. 2017.
[83] M. W. A. Khan, E. Moradi, L. Sydänheimo, T. Björninen, Y. Rahmat-Samii, L. Ukkonen, "Miniature co-planar implantable antenna on thin and flexible platform for fully wireless intracranial pressure monitoring system," *Intl. J. Antennas Propag.*, Article ID: 9161083, 9 pages, Jan. 2017.
[84] Z. Xiao et al., "An Implantable RFID Sensor Tag toward Continuous Glucose Monitoring," *IEEE Journal of Biomedical and Health Informatics*, vol. 19, no. 3, pp. 910-919, May 2015.
[85] H. Huang et al., "RFID Tag Helix Antenna Sensors for Wireless Drug Dosage Monitoring," *IEEE Journal of Translational Engineering in Health and Medicine*, vol. 2, pp. 1-8, 2014, Art no. 1700108.
[86] T. Volk et al., "RFID Technology for Continuous Monitoring of Physiological Signals in Small Animals," *IEEE Transactions on Biomedical Engineering*, vol. 62, no. 2, pp. 618-626, Feb. 2015.

[87] T. Björninen, L. Sydänheimo, L. Ukkonen, "Development and validation of an equivalent circuit model for UHF RFID IC based on wireless tag measurements," in AMTA Symp., Bellevue, WA, USA, 2012.
[88] S. Ma, L. Sydänheimo, L. Ukkonen and T. Björninen, "Electrically Small UHF RFID Tag Antenna Based on Inductively Coupled Resonant LC Tank," in Asia-Pacific Microwave Conference 2019, Singapore, 2019.
[89] M. Kiani and M. Ghovanloo, "The circuit theory behind coupled-mode magnetic resonance-based wireless power transmission," *IEEE Trans. Circuits Syst*. I Regul. Pap., 2012, vol. 59, no. 9, pp. 2065–2074.
[90] L. Xu, Y. Guo and W. Wu, "Miniaturized Circularly Polarized Loop Antenna for Biomedical Applications," *IEEE Transactions on Antennas and Propagation*, vol. 63, no. 3, pp. 922-930, 2015.
[91] H. Li, Y. Guo, C. Liu, S. Xiao and L. Li, "A Miniature-Implantable Antenna for MedRadio-Band Biomedical Telemetry," *IEEE Antennas and Wireless Propagation Letters*, vol. 14, pp. 1176-1179, 2015.
[92] L. Xu, Y. Guo and W. Wu, "Miniaturized Dual-Band Antenna for Implantable Wireless Communications," *IEEE Antennas and Wireless Propagation Letters*, vol. 13, pp. 1160-1163, 2014.
[93] C. Liu, Y. Guo and S. Xiao, "Capacitively Loaded Circularly Polarized Implantable Patch Antenna for ISM Band Biomedical Applications," *IEEE Transactions on Antennas and Propagation*, vol. 62, no. 5, pp. 2407-2417, 2014.
[94] Kim, J. and Rahmat‐Samii, Y., "Planar inverted‐F antennas on implantable medical devices: Meandered type versus spiral type," *Microw. Opt. Technol. Lett.*, 48: 567-572, 2006.
[95] C. Liu, Y. Guo, H. Sun and S. Xiao, "Design and Safety Considerations of an Implantable Rectenna for Far-Field Wireless Power Transfer," *IEEE Transactions on Antennas and Propagation*, vol. 62, no. 11, pp. 5798-5806, 2014.
[96] T. Karacolak, A. Z. Hood and E. Topsakal, "Design of a Dual-Band Implantable Antenna and Development of Skin Mimicking Gels for Continuous Glucose Monitoring," *IEEE Transactions on Microwave Theory and Techniques*, vol. 56, no. 4, pp. 1001-1008, 2008.
[97] Z. Duan, Y. Guo, M. Je and D. Kwong, "Design and in Vitro Test of a Differentially Fed Dual-Band Implantable Antenna Operating at MICS and ISM Bands," *IEEE Transactions on Antennas and Propagation*, vol. 62, no. 5, pp. 2430-2439, 2014.
[98] A. M. Sodagar and P. Amiri, "Capacitive coupling for power and data telemetry to implantable biomedical microsystems," in *Proc. IEEE 4th Int. Conf. Neural Eng.*, pp. 411–414, 2009.
[99] R. Jegadeesan et al., "Wireless Power Delivery to Flexible Subcutaneous Implants Using Capacitive Coupling," *IEEE Transactions on Microwave Theory and Technique*, vol. 65, no. 1, pp. 1-13, 2017.
[100] R. Narayanamoorthi, "Modeling of Capacitive Resonant Wireless Power and Data Transfer to Deep Biomedical Implants," *IEEE Transactions on Components, Packaging and Manufacturing Technology*, vol. 9, no. 7, pp. 1253-1263, 2019.
[101] R. Bercich et al., "Far-field RF powering of implantable devices: Safety considerations," *IEEE Trans. Biomed. Eng.*, vol. 60, no. 8, pp. 2107–2112, 2013.